SAND2023-08836J

X-ray Self-Emission Imaging with Spherically Bent Bragg Crystals on the Z-machine

E.C. Harding[1], G.K. Robertson, G.S. Dunham, M.R. Gomez, J.R. Fein, P.F. Knapp, A.J. Harvey-Thompson, C.S. Speas, D.J. Ampleford, G.A. Rochau

Sandia National Laboratories, Albuquerque, New Mexico 87185, USA

R. Doron and Y. Maron

Weizmann Institute of Science, Rehovot 7610001, Israel

[1]The author to whom correspondence may be addressed: ehardi@sandia.gov

ABSTRACT

An x-ray imaging scheme using spherically bent crystals was implemented on the Z-machine to image x-rays emitted by the hot, dense plasma generated by a Magnetized Liner Inertial Fusion (MagLIF) target. This diagnostic relies on a spherically bent crystal to capture x-ray emission over a narrow spectral range (<15 eV), which is established by a limiting aperture placed on the Rowland circle. The spherical crystal optic provides the necessary high-throughput and large field-of-view required to produce a bright image over the entire, one-centimeter length of the emitting column of plasma. The average spatial resolution was measured and determined to be 18 μm for the highest resolution configuration. With this resolution, the radial size of the stagnation column can be accurately determined and radial structures, such as bifurcations in the column, are clearly resolved. The success of the spherical-crystal imager has motivated the implementation of a new, two-crystal

configuration for identifying sources of spectral line emission using a differential imaging technique.

I. INTRODUCTION

Inertial confinement fusion (ICF) involves small, laboratory-scale implosions that briefly compress hydrogen fuel into a hot, dense thermonuclear plasma. During peak compression the fusing plasma emits a burst of neutrons, x-rays, and gamma rays over a nanosecond or less and originate from complex volumes with scale sizes of 10 to 100 μm. The overall size and the internal structure of the emitting plasma is measured by imaging this radiation. This enables an assessment of the compression uniformity, and a detailed comparison to simulations with the ultimate goal of maximizing the neutron output from thermonuclear reactions. In most cases, the overall size of the emitting plasma is roughly 100 μm in the implosion direction, which necessitates an image resolution of 10 μm or better. While imaging the spatial distributions of the neutron or gamma ray products from the fusion reactions is ideal, and currently possible [1], no time-resolved detection techniques are feasible at present. On the other hand, soft x-rays ($h\nu$ ~10 keV) emitted by electrons in the plasma are energetic enough to emerge from the plasma and are easily captured with time-gated detectors (e.g., microchannel-plate-based framing cameras [2]). The origin of these x-rays is not limited to the neutron producing regions, but if interpreted carefully, their spatial distributions can provide critical insight into implosion performance. Thus, x-ray imaging is an important diagnostic for nearly all ICF concepts.

Currently, a magneto-inertial fusion concept known as Magnetized Liner Inertial Fusion, or MagLIF, is being pursued on Sandia's large pulsed-power device known as the Z-machine [3, 4]. A typical MagLIF target consists of a cylindrical, beryllium tube (referred to as a "liner") that

has an active length of 10 mm with an inner diameter of 4.65 mm and a wall thickness of 0.465 mm. The tube is filled with deuterium gas (D_2), pre-magnetized [5], pre-heated [6, 7], and then imploded radially inward by directly coupling the electrical current from the Z-machine to the outside surface of the liner. The implosion converges onto the axis of the liner causing rapid heating of the fuel, which leads to a short burst of x-rays lasting 1 to 2 ns during an event known as "stagnation". Previous MagLIF experiments have produced DD neutron yields up to 1.1×10^{13} and peak ion temperatures of 3 keV [8].

The stagnation event forms a narrow column of x-ray emitting plasma that is 6 to 8 mm tall with an average width of around 100 μm [9, 10]. The column is challenging to image because it requires high sensitivity and high spatial resolution over a large, 1-cm vertical field-of-view. A high sensitivity is required due to a relatively weak emission per unit height of the column. This is unlike the more compact capsule implosions in which the entire source is concentrated inside a spherical region with a diameter of approximately 100 microns or less [11, 12]. To meet these requirements, we implemented a reflective-optic imaging diagnostic that relies on a single, spherically bent crystal to image x-rays (see Figure 1) with a magnification of 6x.

We also discovered that we could exploit the narrow bandpass provided by the crystal reflection to differentiate spectral-line emission from the broadband continuum emission. This provided a way to track the location of thin, elemental coatings applied to the liner. As a result, we can now visualize the mixing that occurs between the imploding liner and the hot D fuel at stagnation,

similar to that first proposed in [13]. This technique represents an important advancement for MagLIF and should benefit other ICF concepts.

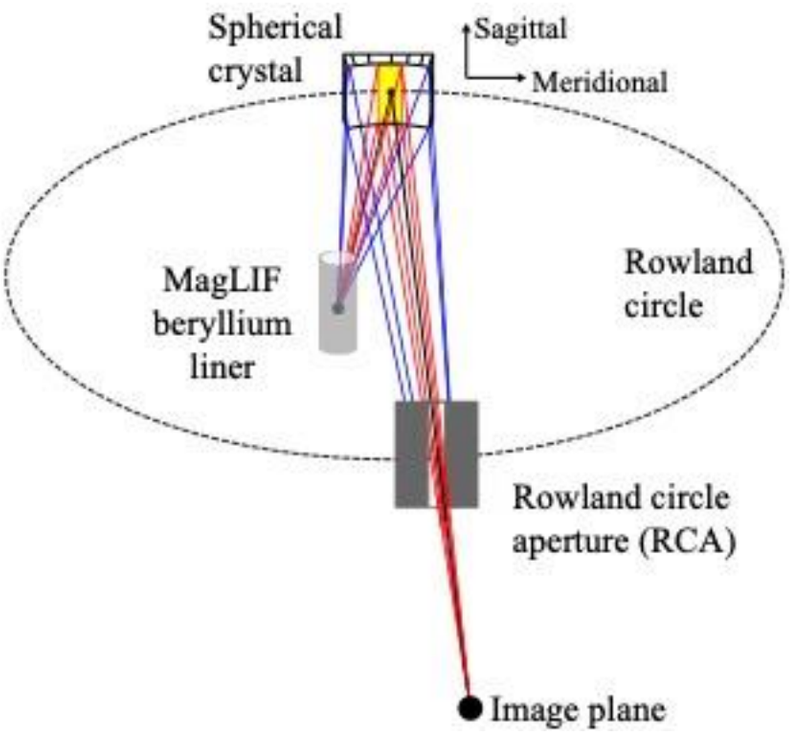

Figure 1. A spherical-crystal imaging geometry operating at near-normal reflection. In this sketch the point source is emitting at all photon energies allowing the entire crystal to participate in the reflection. The Rowland circle aperture then limits which rays reach the image plane. The blue colored rays are stopped by the aperture, while the red rays pass through. The yellow area on the crystal face is responsible for reflecting the red rays.

II. BACKGROUND

In early MagLIF-like experiments, monochromatic backlighting was routinely used to diagnose the in-flight stability of the imploding liner [14, 15]. In the backlighting configuration the target is placed between a small, point-like x-ray source and a spherically bent crystal. The x-rays emitted by the point source are differentially absorbed as they pass through the target and the transmitted x-rays form a radiograph, which is then captured by the crystal optic and imaged over a narrow energy range [16-18]. The present work builds on the success of the backlighter technique by using similar alignment and fielding strategies but with the goal of directly imaging

the x-rays produced by the target, commonly referred to as "self-emission". This method of imaging with spherical crystals was first demonstrated in the 1970's [19] and more recently in a variety of experiments [16, 20-22]. Despite successful demonstrations and advantages argued by Koch *et. al.* [23], self-emission imaging with spherical crystals was not widely implemented due to resolution limitations and the relatively high-fielding complexity compared to pinhole cameras. In general, the ultimate resolution is limited by optical aberrations, namely astigmatism, which make it challenging to achieve resolutions below 10 μm. Achieving higher resolutions requires more complex, aspherical shapes (e.g., toroidal [24]), or other imaging methods such as Kirkpatrick-Baez microscopy [25, 26], penumbral imaging [27], or Fresnel zone-plate imaging [28]. All these methods are attractive options for applications that require high-resolution (<10 μm) and a small field-of-view (FoV < 1 mm).

Despite the resolution limitations, spherical crystals have several advantages over other imaging techniques that make them well-suited for imaging the high-aspect-ratio MagLIF stagnation column. Primarily, they can maintain a nearly constant collection efficiency over a large, 1-cm, FoV. MagLIF also benefits from the narrow spectral window provided by the crystal reflection. This allows the creation of images whose spectral content is dominated by line emission or continuum within a narrow spectral range. This is a valuable attribute and is described in Section IV D. Finally, there are several practical considerations regarding the routine fielding of a spherical crystal imager in the harsh Z-Machine environment. First, the reflection geometry eliminates the direct line-of-sight from the target to the detector. This allows us to simultaneously shield the detector from shot debris and reduce the hard x-ray background ($h\nu \sim 1$ MeV) on the detector. Secondly, it is nearly impossible to protect the crystal from shot debris at the soft x-ray

energies considered here. As a result, the crystal is destroyed during every experiment making aspherical shapes prohibitively expensive.

III. DESIGN

This section describes the theoretical operation of a spherical-crystal imager. The intent is to provide a detailed description along with several key equations to allow the reader to design an imager suitable for their application. Much of the operation is similar to the backlighting configuration. However, a self-emission imager must use an aperture to control the spectral content of the image.

A. Magnification and Image Distance

The spherical crystal generates a spectral-like reflection that forms an image in a manner that is similar to a common optical mirror. However, at x-ray wavelengths, the reflection is generated by the diffraction of x-rays within the volume of the crystal lattice and is highly peaked when the reflection angle satisfies Bragg's equation,

$$n\lambda = 2d \sin \theta_B \tag{1}$$

Here n is the reflection order, λ is the x-ray wavelength, d is the spacing of the crystal's atomic planes, and θ_B is the reflection angle, or Bragg angle, which is measured with respect to the surface

of the mirror. All crystals were fabricated such that the orientation of the atomic planes, which are identified by the Miller indices (hkl), are aligned parallel to the surface of the crystal, making it a symmetric reflection. The crystal optic was fabricated by forcibly contacting a thin crystal wafer (50 to 100 μm thick) to a concave glass backing that has the desired radius of curvature.

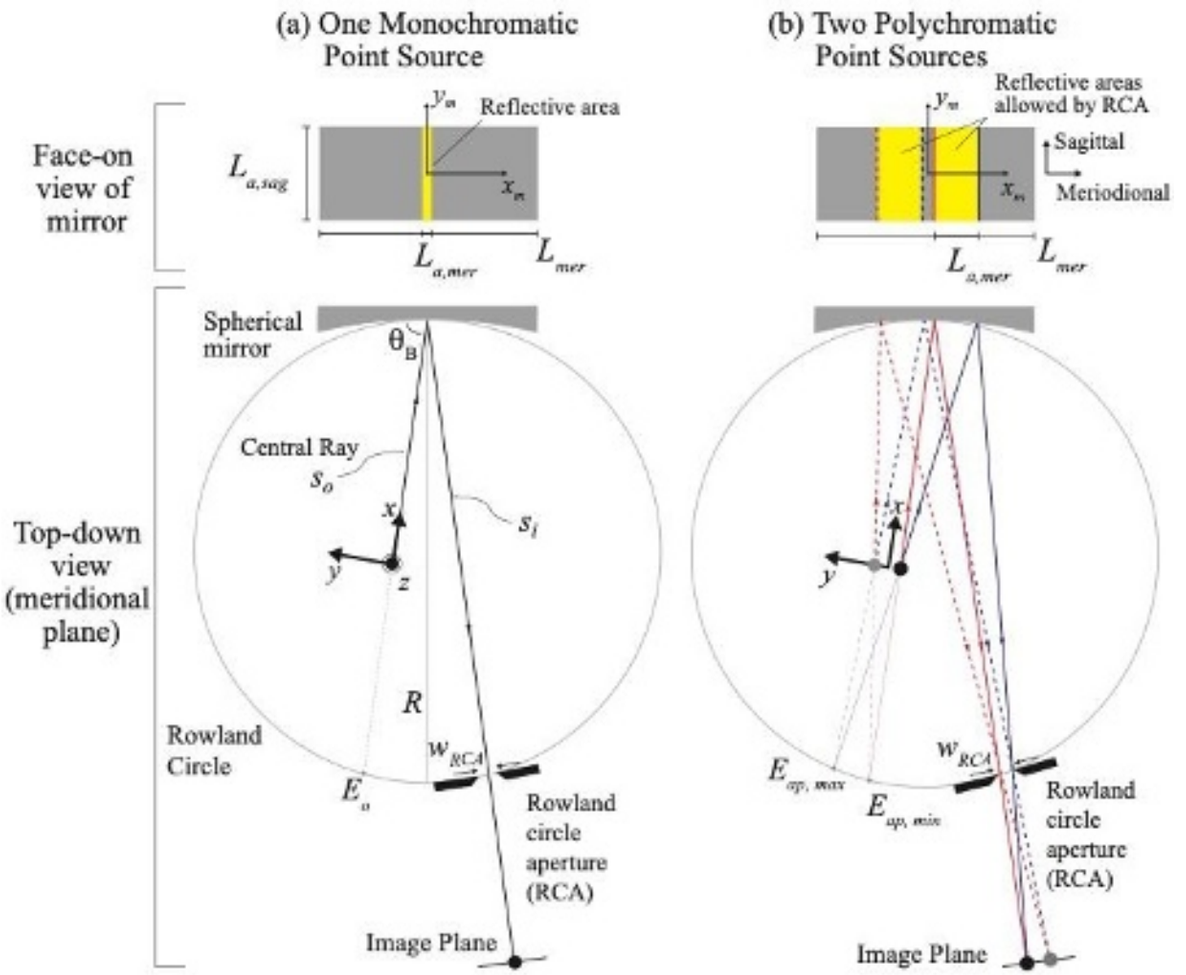

Figure 2. *Schematics of a spherical-crystal imager that illustrate the differences between monochromatic and polychromatic sources and the use of a Rowland circle aperture. In both cases, the active height of the crystal ($L_{a,\,sag}$) is equal to the physical height. Object plane coordinates are given as (x,y,z) and mirror coordinates are (x_m, y_m, z_m). (a) A single, monochromatic point source. The width of the mirror's reflective area, defined as $L_{a,\,mer}$, is determined by the imaging geometry and the width of the crystal rocking curve. In this case, the RCA does not limit the rays reaching the image plane (b) Two-point sources separated in the meridional plane that emit over all photon energies. A Rowland circle aperture limits the minimum and maximum photon energies ($E_{ap,\,min}$ and $E_{ap,\,max}$) that reach the image plane and thus controls $L_{a,\,mer}$. The meridional focusing nature of the source is shown here only for illustrative purposes. In practice, the detector is located between the meridional and sagittal focus positions. Note that the reflective areas on the crystal face (yellow-colored regions) are typically curved as shown in Figure 3.*

The focusing behavior of the spherical crystal is similar to an optical mirror and is approximated by the thin lens equation,

$$\frac{1}{s_o} + \frac{1}{s_i} = \frac{1}{f} \tag{2}$$

where s_o is the object-to-crystal distance, s_i is the crystal-to-image distance, and f is the focal length of the mirror. The focal length has two values, which are

$$f_{sag} = \frac{R}{2 \sin \theta_B} \; and \tag{3}$$

$$f_{mer} = \frac{R \sin \theta_B}{2}, \tag{4}$$

where f_{mer} and f_{sag} are the focal lengths in the meridional and sagittal planes, respectively, and R is the radius of curvature. The separation of the focal lengths is a result of the off-axis imaging geometry necessary for Bragg reflection. This generates two characteristic image planes, each with a unique best-focus position. As shown in Figure 2 the meridional plane contains both the incident and reflected rays. It also contains the Rowland circle (RC), an imaginary circle that has a diameter equal to the radius of the crystal [29]. The RC has important properties that describe the dispersion and focusing of x-rays in the meridional plane. Namely, all x-rays emitted from a point source on the RC will strike the crystal with nearly the same incident angle and will thus be reflected with nearly identical efficiencies. Since the incident angle varies along the RC, so does the energy that satisfies the Bragg condition at each point on the RC. As a result, each point along the RC corresponds to a unique photon energy available for imaging, but only if that photon energy is emitted by the source, and a straight line connects three points: (1) a point on the RC, (2) a point on the source, and (3) a point on the crystal as shown in Figure 2 (a) and (b).

The sagittal plane is orthogonal to the meridional plane, and to first order no change in incident angle occurs in this plane if $L_{sag}/s_o << 1$. Relative to the MagLIF target, the sagittal plane is parallel to the cylindrical axis of the liner and thus vertically orientated. The meridional plane is orthogonal to the cylindrical axis of the liner and therefore horizontally orientated. The resolution provided by the meridional focusing is used to resolve the radial size of the stagnation column.

The magnifications in the two planes are,

$$M_{sag} = \frac{s_i}{s_o} \ and \tag{5}$$

$$M_{mer} = \frac{s_i - R\sin\theta_{\boldsymbol{B}}}{s_o - R\sin\theta_{\boldsymbol{B}}}, \tag{6}$$

where a negative M_{mer} value indicates that the image is inverted in the meridional plane. The image is always inverted in the sagittal plane, and we therefore omit the minus sign in Eq. 5. The magnifications are not equal, but for the MagLIF configurations discussed here the difference is less than 5% in all cases.

A. Spatial Resolution

In most cases, the theoretical spatial resolution of a spherical crystal imager is limited by astigmatism. The resolution may be further degraded by form errors in the surface shape or microstructure damage from polishing. Both of these effects may limit the ultimate resolution for even complex aspherical shapes designed to reduce astigmatism [30]. An estimate of the astigmatism-limited resolution was derived in [23] and is given here as,

$$\sigma = L(1 - \sin\theta_B)\frac{M+1}{M} \tag{7}$$

where M is an average spatial magnification and L is the size of the active crystal aperture, which may be approximated as $(L_{a,sag} + L_{a,mer})/2$ in cases where $L_{a,sag} \neq L_{a,mer}$. This equation assumes the detector is positioned so that the sagittal and meridional resolutions are the same. While not intended for detailed resolution calculations, this equation confirms that a small active crystal size and a large Bragg angle are required to achieve a high resolution. In practice, we rely on ray-tracing to estimate the overall point spread function (PSF) in the detector plane. The calculated PSF is then rescaled in the sagittal and meridional directions by factors $1/M_{mer}$ and $1/M_{sag}$, respectively, to give the PSF in the object plane. The resolution of the imager is then defined as the full width at half-maximum (FWHM) of the object-plane PSF. Typically, the best resolutions are on the order of 10 microns.

To achieve spatial resolutions that are equal in both the meridional and sagittal planes a symmetrical PSF must be produced at the image plane. This is accomplished by setting $s_i = s_i^{sym}$, where,

$$s_i^{sym} = \frac{s_o(1+\beta)R\sin\theta_B}{2s_o(\sin^2\theta_B + \beta) - (1+\beta)R\sin\theta_B}. \quad (8)$$

Here $\beta = L_{a,mer} / L_{a,sag}$ where $L_{a,mer}$ and $L_{a,sag}$ are the dimensions of the mirror area that is used for imaging in the meridional and sagittal directions, respectively (see Figure 2). For the case of $\beta = 1$, s_i^{sym} is approximately $s_oR/(2s_o - R)$. This locates the image plane approximately halfway between the meridional and sagittal focuses at a position known as the circle of least confusion, which was the assumed position for Eq. 8. As shown in Figure 2, the imaging configurations developed for MagLIF use crystals with rectangular shapes, and have $\beta < 1$, yielding a larger s_i^{sym} value that places the detector closer to the sagittal focus than to the meridional focus. In practice,

computational ray-tracing should be carried out to further optimize the detector position since Eq. 8 is only an approximation.

B. Image Bandwidth and Field-of-View

The reflected rays from a spherical-crystal have a well-defined energy range, ΔE, and central energy, E_o, that define a so-called spectral window through which the detector views the target. The ratio of these quantities is referred to as the image bandwidth and is approximated (assuming $L_{a,mer} << s_o$) by the following equation,

$$\frac{\Delta E}{E_o} = \frac{L_{a,mer}}{R}\left|\frac{s_0 - R\sin\theta_B}{s_0}\right|\cot\theta_B \tag{9}$$

[31]. Here again E_o is the central x-ray energy, which is reflected by the center of the crystal, and $\Delta E = E_{max} - E_{min}$, where E_{max} and E_{min} are the maximum and minimum energies, which are determined by the active width of the crystal (i.e., $L_{a,mer}$). The maximum value for ΔE occurs when the entire crystal width participates in the reflection (i.e., $L_{a,mer} = L_{mer}$). However, this is not always a desirable configuration.

The values of ΔE and E_o will deviate from Eq. 9 due to changes in incident angle when the source is moved in the meridional or sagittal directions away from the central-ray location. The incident angle changes are most severe for source movements in the meridional plane (i.e., along the y-axis as defined in Figure 2). This is not a desirable effect and may not be tolerable if the spectral window must remain centered on a spectral line. To solve this problem, a limiting aperture is placed at the RC position along the reflected ray path as shown in Figure 1 and 2, recognizing again that the position of the reflected ray at the RC corresponds to a specific photon energy. We call this aperture the Rowland circle aperture (RCA). The operation of the RCA was first described in [32]. The RCA only accepts rays within an energy range that is defined by the aperture's

location and width. It effectively fixes the spectral window so that ΔE and E_o remain constant for all source locations without limiting the horizontal or vertical FoV. This fact makes an RCA essential for nearly all applications of a spherical-crystal imager.

The relationship between the width of the RCA, w_{RCA}, and $L_{a,mer}$ is given by,

$$w_{RCA} = L_{a,mer} \sin\theta_B \left(\left| \frac{R \sin\theta_B}{s_o} - 1 \right| \right). \tag{10}$$

Solving for $L_{a,mer}$ and inserting into Eq. 8 we find that the bandwidth allowed by the aperture is,

$$\frac{\Delta E_{ap}}{E_o} = \frac{w_{RCA}}{\mathrm{R} \sin\theta_B \tan\theta_B}. \tag{11}$$

where $\Delta E_{ap} = E_{ap,\,max} - E_{ap,\,min}$. $E_{ap,\,max}$ and $E_{ap,\,min}$ are the maximum and minimum energies allowed to pass through the aperture. As an example, the standard high-resolution imaging configuration on the Z-machine has R = 250 mm, $\theta_B = 86°$, w_{RCA} = 2.3 mm, which gives ΔE_{ap} = 4.0 eV for the n = 2 reflection and 6.0 eV for the n = 3 reflection. This means the position of the RCA can be displaced by 0.6 mm and E_o will only change by approximately 1 eV for the n = 2 reflection.

In order for the RCA to maintain a fixed spectral window over the entire FoV, the meridional size of the crystal must be larger than the active portion of the crystal (i.e., $L_{mer} > L_{a,mer}$), which is the case shown in Figure 2. This condition is necessary because as the emission point moves in the meridional plane it must use a different portion of the crystal to maintain a Bragg reflection, or equivalently a range of incident angles, that is accepted by the RCA. This is shown in Figure 2

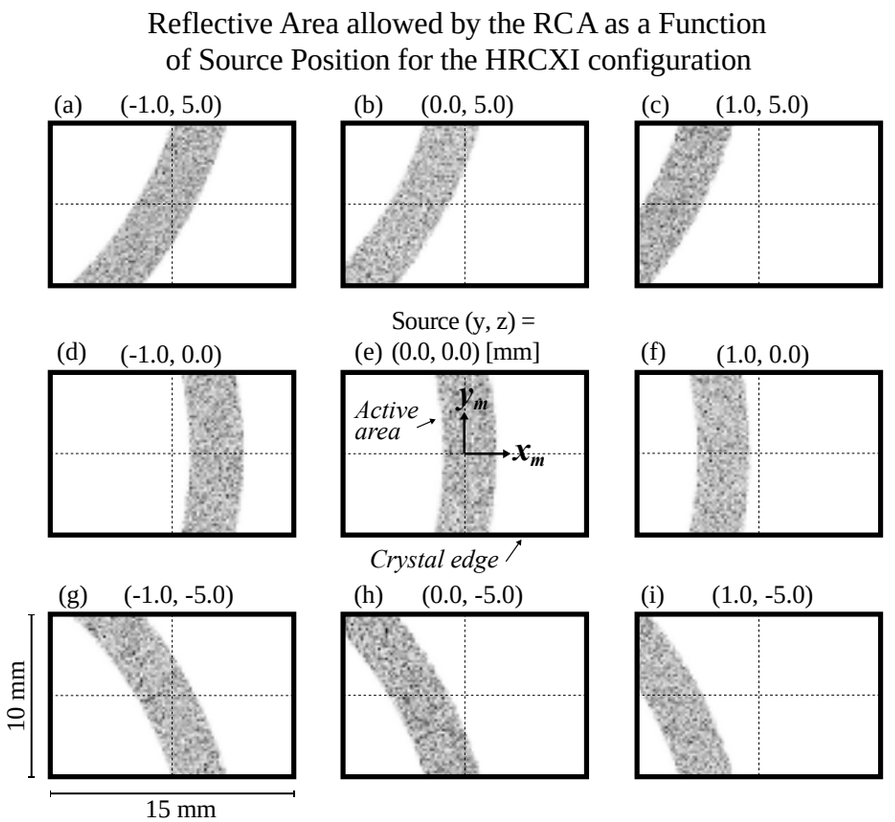

Figure 3. (a)-(i) SHADOW3 ray-tracing results that show the reflective areas allowed by the RCA on the crystal face for nine different source locations in the (y, z)-object plane for a specific configuration known as the HRCXI. The effects of the crystal rocking curve are included but are negligible and do not impact the overall shape. Source (x, y, z) and mirror (x_m, y_m, z_m) coordinates are defined in Figure 2. The intersection of the dashed lines indicates the center of the crystal. The changes in the reflective portion shown here led to variations in the throughput, resolution, and field-of-view.

(b) where the left point source uses a portion of the crystal that is located further to the left compared to the portion used by the right point source. Figure 3 illustrates this effect for an array of source of locations that define the limits of the required FoV for a common MagLIF configuration. Figure 3 (d), (e), and (f), show the movement of the reflective area for source positions at -1, 0, and +1 mm along the y-axis respectively. As the source continues to translate to even greater distances, the reflective area slides off the edge of the crystal causing an effective reduction in ΔE and a corresponding roll-off in the image intensity. This effect is referred to as chromatic vignetting.

The meridional FoV was defined based on the source position where the active area reaches the edge of the crystal. The meridional FoV is therefore determined by the relative sizes of $L_{a,mer}$ and L_{mer}, and is found by tracing the edges of the Rowland circle aperture to the edges of the crystal in the meridional plane. The meridional FOV is then approximated by,

$$FoV_{mer} = \frac{s_o - R\sin\theta_B}{R\sin\theta_B}\left(\frac{L_{mer}}{\sin\theta_B} - L_{a,mer}\right) \quad (12)$$

Comparably, a loss of spatial resolution could also limit the FoV, yet for the imagers presented here the spatial resolution does not rapidly degrade near the edges of the FoV making image intensity the more sensible parameter for defining the FoV.

Defining the FoV in the sagittal direction is more complicated. As the source moves up and down in the sagittal plane, the active portion of the crystal moves diagonally across the crystal surface as seen in the top and bottom rows of Figure 3. Similar to the meridional plane, the active area eventually slides off the crystal causing vignetting of the image. If the RCA is simply a slit oriented in the sagittal direction (as shown in Figure 1), this will result in the center energy of the spectral window shifting as the emission point moves up or down in the sagittal plane. Alternatively, the center energy can be made to remain fixed as a function of sagittal source position by shaping the RCA to be an annulus, whose width is given by Eq. 10 for a chosen bandwidth. This type of curved RCA is desirable for imaging the MagLIF stagnation column, which has a large extent in the sagittal direction.

In the previous discussion we assumed the source spectrum had a uniform intensity across all photon energies. We now consider imaging a spectral line that has an average brightness that is much greater that of the underlying continuum and may occupy only a fraction of the spectral window allowed by the RCA. Most spectral imaging configurations on Z are setup with $\Delta E_{ap} >$

ΔE_s so that possible shifts in the line center due to plasma motion (i.e., Doppler effects) do not move the spectral line outside the spectral window. In this case, ΔE is effectively equal to the width of the spectral line and the meridional FOV increases due to the delay of chromatic vignetting relative to the continuum. A value for $L_{a,mer}$ can be estimated by setting $\Delta E = \Delta E_s$ and $E_0 = E_s$ in Eq. 9, where ΔE_s and E_s are the FWHM and center energy of the spectral line, respectively.

In cases where $\Delta E_{ap} < \Delta E_s$ is required, the RCA is used to further reduce the spectral window and improve spatial resolution at the expense of image brightness. This is also the proposed configuration for the x-ray Doppler velocimetry application in which fluid motion is visualized by image intensity changes due to velocity induced line shifts [33] .

Finally, it is important to note that in our discussion so far, we have neglected the effects of the crystal rocking curve. The finite width of the rocking curve allows reflections to occur about small deviations from θ_B. Therefore, even with an infinitely narrow RCA the crystal will produce a bandwidth equal to,

$$\frac{\Delta E_{rock}}{E_0} \approx \frac{\Delta \theta_{rock}}{\tan \theta_B} \tag{13}$$

where $\Delta\theta_{rock}$ is the FWHM of the rocking curve. Typical values for $\Delta\theta_{rock}$ for Quartz, Ge, or Si crystals are on the order of 10^{-4} radians for energies in the 6 to 10 keV range. For $\theta_B = 83°$ this gives $\Delta E_{rock}/E_0 \sim 10^{-5}$, which yields $\Delta E_{rock} = 0.1$ eV at 10 keV. The imaging systems design for the MagLIF target typically use $\Delta E_{ap} = 4$ to 12 eV and in these cases the rocking curve has a negligible effect on the image bandwidth. If ΔE_{rock} becomes comparable to ΔE_{ap}, the image bandwidth will increase and can be estimated as the quadrature sum of ΔE_{rock} and ΔE_{ap} [34].

C. Throughput and Image Fluence

The collection efficiency of the spherical crystal imager is defined by a reflectivity-weighted solid-angle, over which x-rays are reflected from the crystal surface. This active solid angle is referred to as the throughput and is related to the reflective area shown in Figure 3. The noted high-sensitivity of spherical-crystal imagers (e.g., compared to pinhole cameras) is attributed to large throughput values that can easily reach 10^{-5} steradians. To estimate the throughput, the solid angle (Ω) subtended by the crystal face is multiplied by an efficiency factor (η). The equation for the solid angle is approximated as

$$\Omega = \frac{L_{a,sag}\, L_{a,mer} \sin(\theta_B)}{{s_o}^2}, \tag{14}$$

and the efficiency (derived in [34]) is approximated as,

$$\eta = \frac{R_{int}}{\left(\frac{\Delta E_{ap}}{E}\right) tan(\theta_B)} \tag{15}$$

where R_{int} is the crystal integrated reflectivity, and we assumed the bandwidth is limited by the RCA. If a spectral line is present and has a width less than ΔE_{ap}, then ΔE_{ap} should be replaced with ΔE_s. The product $\eta\Omega$ is the throughput or sometimes referred as the active solid angle, Ω_{act}. Because the bandwidth and $L_{a,mer}$ are related by Eq. 9, the throughput is reduced to the following equation:

$$\Omega_{act} = \eta\Omega = \frac{L_{a,sag}}{s_o}\left|\frac{R\sin\theta_B}{R\sin\theta_B - s_o}\right| R_{int} \tag{16}$$

Interestingly, the result is the same as a monochromatic source [31], independent of bandwidth. This means that if the same number photons contained in a monochromatic source are distributed over the energy range, $L_{a,mer}$ increases and the total number of reflected photons remains the same.

In contrast, the throughput is directly proportional to $L_{a,sag}$ since the entire sagittal length participates in the reflection for a single photon energy as presented in Figure 1. In addition, the throughput increases as the source moves closer to the Rowland circle due to an increase in $L_{a,mer}$ without an increase in ΔE. Near the Rowland circle the size of $L_{a,mer}$ may exceed L_{mer} and in this case Eq. 16 is no longer valid. One further limitation is that Eq. 16 applies only to the central ray. From ray tracing we find that the throughput varies depending on the source location due to the change in the active crystal area as a function of source position as shown in Figure 3. In Section IV, we show that the variation is typically less than 20% over a 1-cm height for the MagLIF configurations.

To perform an absolute calibration of the source emission, we give an expression for the image fluence, I_D, which is defined as the energy per unit area on the detector, and is calculated as,

$$I_D \left[\frac{ergs}{cm^2}\right] = \left(\frac{\Omega_{act}\, T_f}{M_{sag}\, M_{mer}}\right) \int I_o(E) dE \tag{17}$$

where T_f is the transmission of the detector filters and $I_o(E)$ is the source brightness with units equal to ergs/(sterdian*eV*cm^2). The integral is evaluated over the bandpass defined by the RCA (ΔE_{ap}) or the spectral line width (ΔE_s). For a flat continuum spectrum, $\int I_o(E) dE = I_o \Delta E_{ap}$. If the crystal yields multiple reflections from different orders, I_D must be calculated for each reflection and then the sum of the individual reflections yields the total image fluence.

D. Depth-of-Field

The depth-of-field (DoF) is a parameter that describes the change in the PSF size when the source-to-crystal distance is varied for a fixed detector position. This is important for understanding the required alignment tolerances, and the loss of resolution that occurs when the source is extended in the source-to-crystal direction. We assume the width of the defocused PSF is the convolution

of three widths: (1) the image size derived from the thin lens equation for small deviations from s_o, (2) the detector resolution element size (w_{det}) scaled to the object plane using M_{mer}, and (3) the PSF width at best focus ($w_{PSF,best}$) scaled to the object plane using M_{mer}. The best focus PSF is assumed to be symmetrical and is found using ray tracing or estimated from Eq. 7. Under these assumptions, the PSF width in the object plane, w_{PSF}, resulting from a variation of object-to-crystal distance, Δs_o, is given as,

$$w_{PSF} = \sqrt{\left(\left(\frac{L_{a,mer}}{s_i M_{mer}}|\Delta s_o|\left(\frac{f_{mer}}{s_o - f_{mer}}\right)^2\right)^2 + \left(\frac{w_{det}}{M_{mer}}\right)^2 + \left(\frac{w_{PSF,best}}{M_{mer}}\right)^2\right)} \quad (18)$$

Equation 18 is for the meridional plane. To estimate the PSF width in the sagittal plane one can simply replace $L_{a,mer}$, M_{mer}, and f_{mer} with $L_{a,sag}$, M_{sag}, and f_{sag}, respectively. To parameterize the DoF with a single value, we define the DoF as the change in object-to-crystal distance that results in a factor of $\sqrt{2}$ change in the PSF width. This results in an approximately 2x change in the PSF intensity. The DoF is small (< 1 mm) for all configurations discussed in a later section and is due to the large collection angle of the active crystal area.

IV. Computational Ray-Tracing

Computational ray-tracing is an important tool for examining the imaging performance of the crystal imager for object positions that are far from the central ray where analytical estimates are less accurate. In particular, we relied upon ray-tracing to quantify the position-dependent resolution and throughput across the desired FoV for MagLIF, which extends +/- 5 mm in the vertical plane (z-direction) and +/- 1 mm in the horizontal plane (y-direction). This was done with two approaches, both used the SHADOW3 ray-racing software [35], for several imaging configurations that will be discussed in more detail in Section V.

First, a synthetic grid image was generated by illuminating a grid with a large-area source placed directly behind the grid. This configuration is advantageous because it is easily realized in the laboratory. Second, a point source was used to systematically step through a large number of object positions and the resulting array of PSF images were cataloged. This approach is more difficult to reproduce in the laboratory due to the required small source size and was not attempted here. Fortunately, the ray-tracing results indicated that the resolution measured from the grid images matched that resolution provided more directly by the PSF images. The 50% intensity contours of several individual PSFs from the three different configurations are shown in Figure 4. In addition, the resolution and throughput information from the individual PSFs can be displayed in a more complete way as shown in Figure 5. This figure shows the resolutions and throughputs plotted as a function of the z-coordinate for three different horizontal positions (y = -1, 0, and 1 mm) for an imaging configuration known as the "Ar-Imager", which is discussed later. Although these plots convey the greatest amount of quantitative information, they do not help one visualize how the image is impacted by variations in the PSF size and shape. For this reason, it is worthwhile to show the synthetic grid images. Figure 6 shows the grid images from the same imaging configurations shown in Figure 4. The grid images from the CXI and Ar-Imager configurations

clearly show unequal resolutions in the vertical and horizontal directions that result from the corresponding asymmetrical PSFs shown in Figure 4.

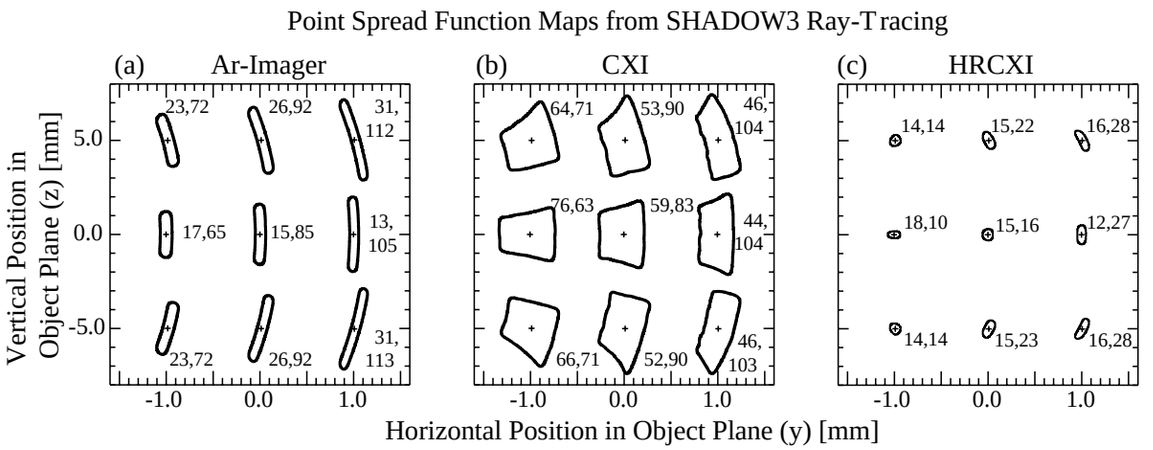

Figure 4. PSF intensity contours from SHADOW3 ray-tracing are shown for three different spherical-crystal imaging configurations: (a) Ar-Imager, (b) CXI, and (c) HRCXI. For all configuratons, the contour values were taken as 50% maximum intensity of each PSF. The '+' symbol marks the intensity-weighted center-of-mass point for the PSF image, which is then mapped to the object plane using M_{mer} and M_{sag}. The contour sizes were increased by 7.5x relative to the axes scale to clearly illustrate the shape of the contour. The image plate resolution (55 μm) was included. The numbers next to each PSF contour are the FWHM values, computed by projecting and summing the PSF intensity values onto the horizontal or vertical axes. The values are presented as 'horizontal, vertical' resolutions with units of μm.

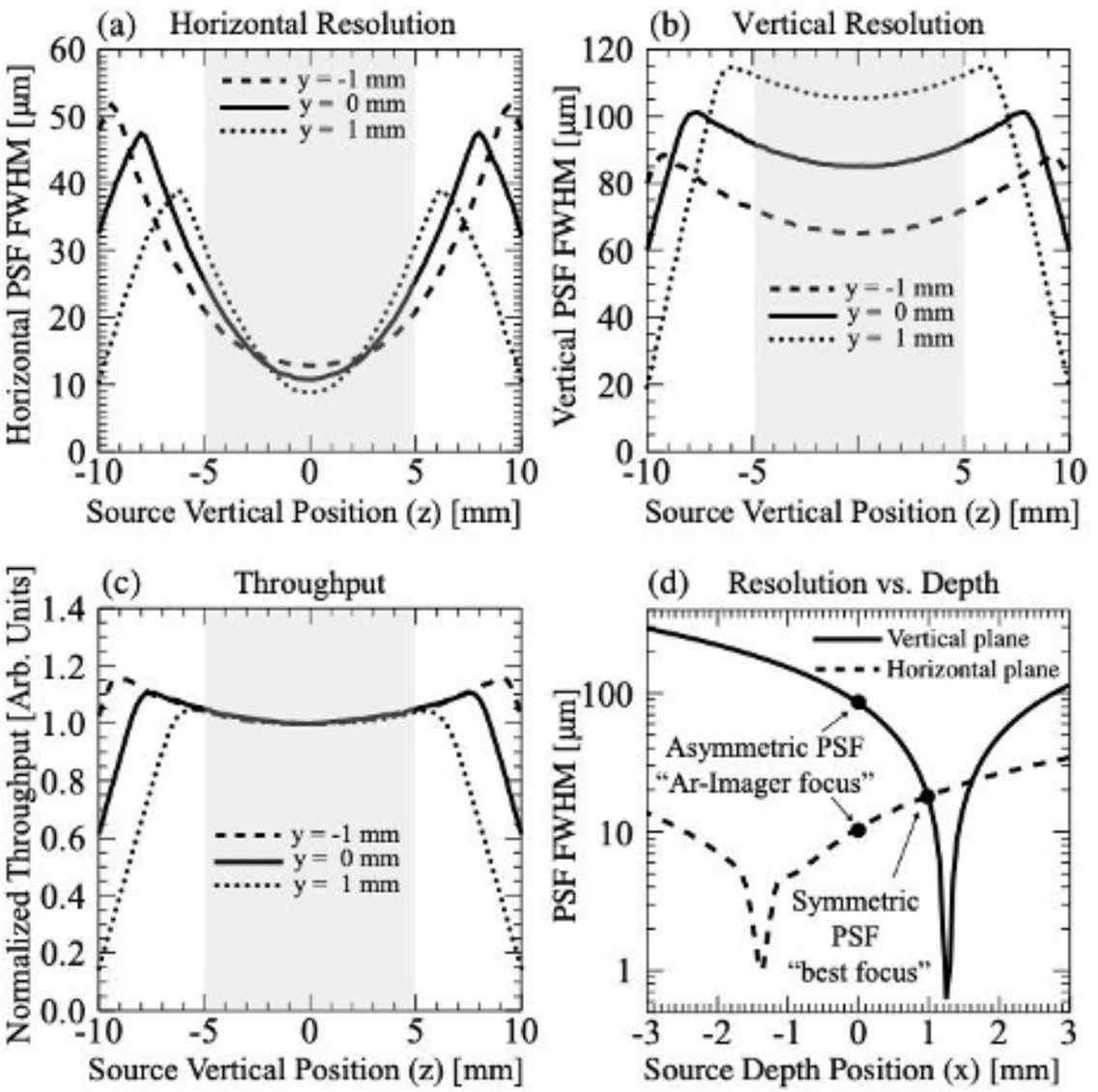

Figure 5. SHADOW3 ray-tracing results for the Ar-Imager configuration using a point source with E_o =3123.2 eV and Gaussian line shape (1.2 eV FWHM). Image plate resolution is not included. (a)(b)(c) Horizontal and vertical resolutions and throughput for different source positions in (y, z)-plane plotted as a function of the z-coordinate (i.e., vertical position) for three horizontal positions: y =-1 ,0, and 1 mm. The throughput was normalized to the z = 0 mm position. The grey shaded regions define the required vertical FoV from z = -5 to 5 mm. (d) Resolution variations for different source positions in source-to-crystal direction (i.e., x-axis or depth position). Source movements toward the crystal are positive values. The Ar-Imager operates with an asymmetric PSF with the source at the x=0 as shown in the plot. Coordinate axes are defined in Figure 2.

In all cases, the crystal rocking curve was generated by the "BRAGG" preprocessor within the SHADOW3 suite of routines. This preprocessor models the crystal in a flat geometry with a finite thickness and does not account for bending effects, which typically lead to an asymmetric

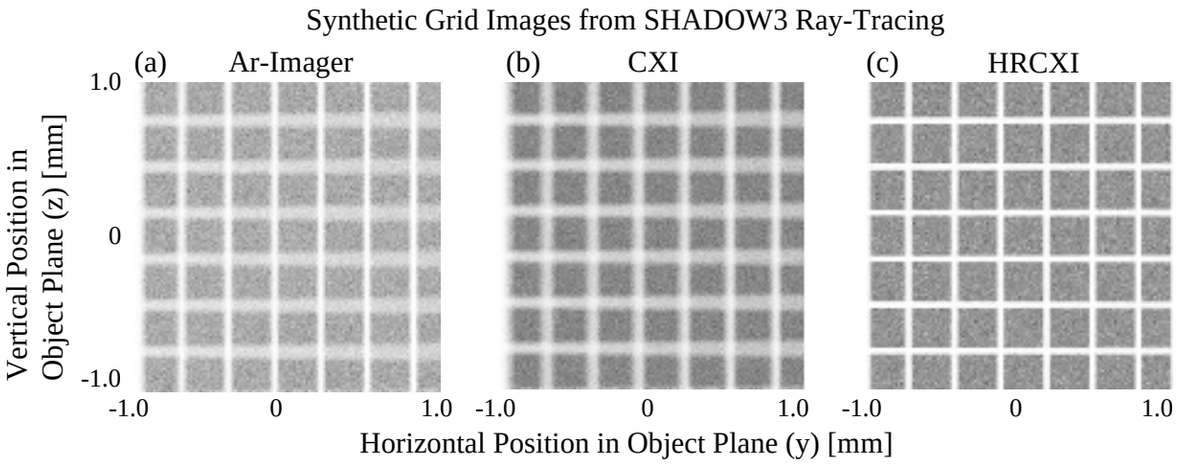

Figure 6. Simulated grid images from SHADOW3 ray-tracing. All grids have a bar width of 40 microns and a period of 300 microns. The grid is illuminatd using a large area source placed directly behind the grid. Grid bars transmit no rays. (a) Ar-Imager configuration using E_o = 3123.2 eV and Gaussian line shape (1.2 eV FWHM), (b) CXI configuration using E_o = 6246.4 eV and a constant intensity (full width = 15.2 eV), (c) HRCXI configuraiton using E_o = 6213.7 eV and a constant intensity (full width = 4 eV).

broadening of the rocking curve. In general, ray-tracing indicated that additional broadening of the rocking curve, as calculated by the XOP Bent-Crystal ML model, does not increase the size of the reflective area of the crystal and therefore does not significantly impact the resolution. The continuum spectrum was modeled as a top-hat function with an intensity equal to one between $E_{min,\,ap}$ and $E_{max,\,ap}$. By doing this the RCA can be removed from the ray tracing allowing us to conserve rays, and yet the effects of the aperture remain accurately modeled. Spectral line sources were modeled by a Gaussian with a FWHM equal to ΔE_s

IV. APPLICATION

In the following sections we discuss several crystal imagers designed for MagLIF experiments. In most cases they were configured for Ar spectral emission or broad-band continuum emission. A

more recent crystal configuration is described in which both Co spectral and continuum emission are imaged simultaneously using two, side-by-side crystals. Detailed ray-tracing calculations using the SHADOW3 software are also shown, and some experimental measurements of the spatial resolution are demonstrated for the primary MagLIF configuration. Shown in Figure 7 is an example of a common assembly that supports all of the crystal imaging configurations. The

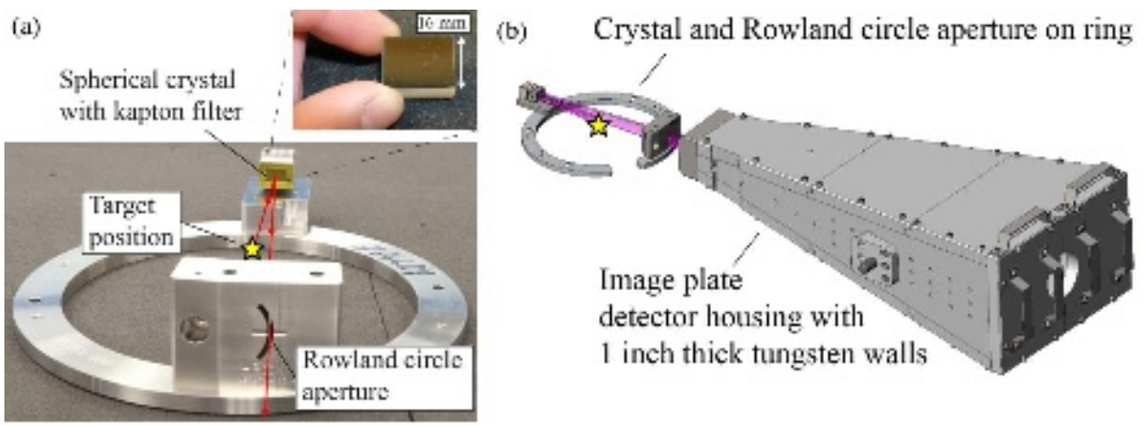

Figure 7. (a) Picture of the crystal imager assembly, known as the HRCXI, before use on the Z-machine. Inset is a close-up picture of the spherically-bent Ge (220) crystal. (b) A rendering of the HRCXI assembly shown with the image plate detector housing. Housing is moved independently of the ring and manually aligned inside the Z vacuum chamber using a visible reflection from the crystal. The purple-colored object represents the x-ray data path.

crystal and RCA are mounted to a ring, which is then attached to the larger target assembly such that the target is in the center of the ring. Figure 8 shows the ring installed in the Z-machine. For all configurations the detector was a Fuji TR Image Plate. Initial experiments used a Fuji-BAS5000 to scan the image plate with an estimated resolution of 63 μm [36]. The signal intensity unit is photo-stimulated light (PSL). Subsequent experiments, which occurred after August 2015, used a DITABIS Super Micron image plate scanner [37] . The resolution of the DITABIS scanner was

modeled as a symmetrical Gaussian with a 55 μm FWHM.

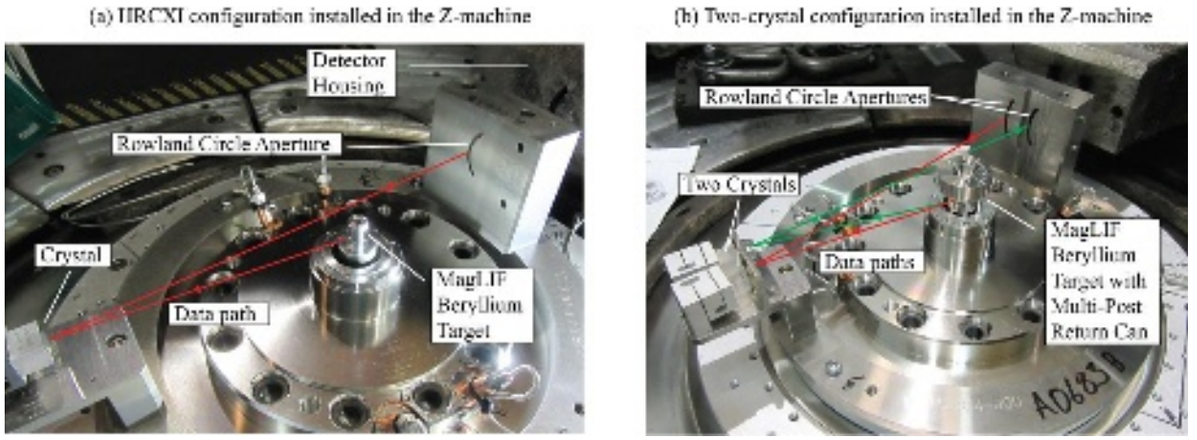

Figure 8. Single and two-crystal imagers installed in the Z-machine. (a) Single configuration known as the HRCXI installed for shot z3120. (b) Two-crystal configuration known as the CHEWI installed for shot z3303. In both configurations the crystals are located 146.6 mm from the target.

	Argon Imager (Ar-Imager)	Continuum X-ray Imager (CXI)	High- Resolution Continuum X-ray Imager (HRCXI)
Emission Type	Ar He_α ($^3P_1$)	Continuum	Continuum
Crystal Plane	Ge (220)	Ge (220)	Ge (220)
Reflection Orders, n	1	1, 2, 3, and 4	1, 2, 3, and 4
2d-spacing [Å]	4.0004	4.0004	4.0004
Center Energies, E_o [eV] for n=1, 2, 3, and 4	3123.2	3123.2, 6246.4, 9369.5, 12492.7	3106.5, 6213.7, 9320.6, 12427.5
Bragg Angle, θ_B	82.91°	82.91°	86.00°
Crystal-to-Image Distance, s_i [mm]	850.0	850.0	854.0
Magnifications: M_{sag} (vertical), M_{mer} (horizontal)	5.797, 5.932	5.797, 5.932	5.825, 5.883
Spectral Window Widths, ΔE_{ap} [eV] for n =1, 2, 3, and 4	7.6	7.6, 15.2, 22.8, 30.4	2.0, 4.0, 6.0, 8.0
Rowland Circle Aperture (RCA) Width, w_{RCA} [mm]	4.850	4.850	2.296
Active Meridional Crystal Length, $L_{a,mer}$ [mm]	1.11	7.06	3.28
Meridional FOV at z = 0 [mm][1], (y_{min}, y_{max})	5	3	4.4
Theoretical Resolution with Image Plate: horizontal (y) x vertical (z). [μm][2]	15 x 85	59 x 83	15 x 16
Theoretical Integrated Reflectivity, R_{int} [mrad][3] for n = 1, 2, 3, and 4	1.02	1.02, 0.23, 0.16, 0.02	1.90, 0.41, 0.30, 0.03
Theoretical Rocking Curve FWHM [mrad][3] for n = 1, 2, 3, and 4	1.05	1.05, 0.21, 0.33, 0.26	1.95, 0.38, 0.57, 0.47
Active Solid Angle, Ω_{act}, [steradians][4] for n = 1, 2, 3, and 4	1.72e-4	1.72e-4, 3.80e-5, 2.73e-5, 3.17e-6	3.16e-4, 6.84e-5, 4.97e-5, 5.63e-6
Typical Detector Filtering	50 μm Be	50 μm Be + 100 μm Kapton HN	50 μm Be + 100 μm Kapton HN + 500 μm Polyimide

[1]Calculated with SHADOW3 ray-tracing software. Here the meridional FOV is defined as the total distance along the horizontal direction (y) over which the full bandwidth is maintained at z = 0 mm. At other z-locations, the meridional FOV may be reduced by vignetting. For smaller bandwidths the meridional FoV increases as demonstrated by the Ar-Imager.
[2]Calculated with SHADOW3 using a point source. For all configurations the Image Plate resolution was included and taken as 55 μm.
[3]The rocking curve was calculated using Bent Crystal ML in XOP v2.4. The following parameters were used in that calculation: temperature factor = 0.9, crystal thickness = 70 μm, Poisson ratio = 0.28 for Ge, and Poisson ratio = 0.22 for Si.
[4]Calculated using Eq. 16 and the R_{int} values listed in this table. Values do not include detector filtering.

Table 1. *Operating parameters for the Ar-Imager, CXI, and HRCXI spherical-crystal imaging configurations. For the Ar-Imager the $L_{a,mer}$, FoV, and resolution values were calculated using a spectral line width equal to 1.2 eV FWHM. CXI and HRCXI values were calculated using the full bandwidth allowed by the RCA. The crystal radius-of-curvature, R, the object-to-crystal distance, s_o, and the crystal size (L_{mer} x L_{sag}) are the same for all configurations and are as follows: R = 250 mm, s_o = 146.615 mm, and L_{mer} x L_{sag} = 15 x 10 mm. All configurations maintain a vertical FoV of 10 mm. The n = 1 reflection in the CXI and HRCXI is blocked by the walls of the Be liner and the detector filter and is listed here only for reference purposes.*

A. Argon Imaging

To investigate the laser pre-heat phase of the MagLIF experiments, dedicated, "laser-only" experiments were conducted in which the laser and applied B-field were present but the Be liner was not imploded. In these experiments, Ar K-shell emission was generated by an added Ar-dopant with an atomic concentration of 0.1%, and higher in some cases. The K-shell spectral lines enabled a measurement of the electron temperature [6, 9, 38-40], and provided a bright source of emission for crystal imaging. A spherical crystal imager configuration (denoted the "Ar-Imager") was designed to have a 7.6-eV bandpass centered around the Ar He_α ($^3P_1$) inter-combination line

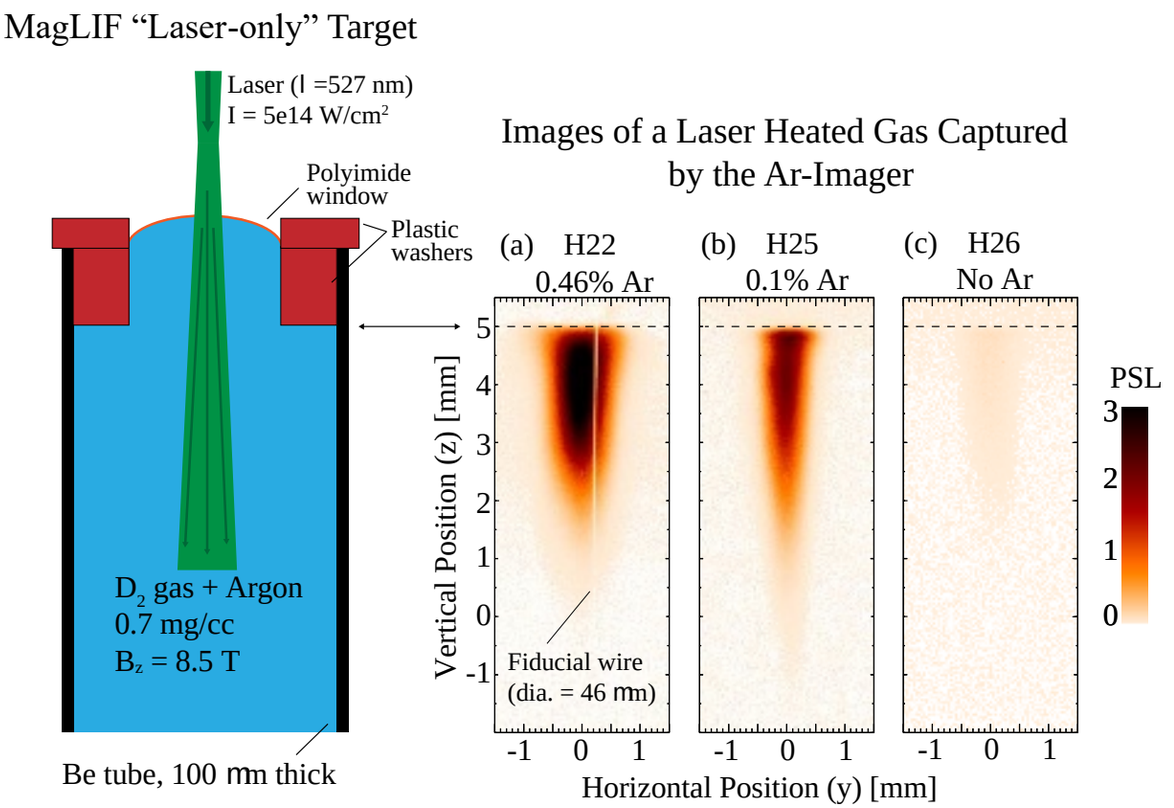

Figure 9. Shown here are three images of laser heated deuterium gas that were captured by a spherical crystal imager known as the Ar-Imager. All shots used an 8.5 T axial B-field, a D_2 gas density equal to 0.7 mg/cc, a Be tube with a wall thickness ~ 100 μm, a 1.5 μm thick polyimide laser-entrance-window, and an unconditioned (i.e., using no distributed phase plate) laser spot focused 5 mm above the entrance to the Be tube. These images were scanned with a Fuji-BAS5000 image plate scanner. The signal intensity unit is photo-stimulated light (PSL). (a) Shot H22 included a 46 μm diameter tungsten wire placed ~3.5 mm from the tube axis and an Ar-dopant concentration equal to 0.46% atomic concentration. The laser setup was as follows: pre-pulse = 416 J / 0.5 ns, 2.7 ns dead time, and main pulse = 3813 J / 4 ns. (b) H25 used a 0.1% atomic Ar-dopant, and the laser setup was as follows: pre-pulse = 496 J / 0.5 ns, 3.6 ns dead time, and main pulse = 2357 J / 2 ns. (c) H26 was identical to H25 except no Ar dopant was added. The laser energy delivered was nearly identical to H25: pre-pulse = 532 J / 0.5 ns, 3.6 ns dead time, and main pulse = 2324 J / 2 ns.

($h\nu$ = 3123.2 eV). It used a Ge (220) crystal plane (2d-spacing = 4.0004 Å) and had a Bragg angle of 82.91°, very similar to the existing backlighter configuration [17, 41], which allowed for a rapid deployment on the Z-machine. Additional properties of the Ar-Imager are listed in Table I.

Figure 9 shows the Ar-Imager data from three laser-only experiments. In these images the laser entered the gas near the top of the target after burning through a thin, polyimide window. Figure 9 (c) shows an un-doped experiment (H26) with a pure D_2 gas fill. The average signal from the un-doped experiment was only 3% of the signal generated in the doped experiment (H25). This proved that the observed signal was dominated by the Ar-dopant and not the continuum emitted by the deuterium.

The estimated intrinsic linewidth of the inter-combination line was between 1 and 1.2 eV FWHM based on the T_e values and spectral resolution reported in [39]. This is much smaller than the 7.6 eV bandpass set by the RCA. Therefore, the linewidth strongly influences the resolution and DoF, as well as the FoV in the horizontal (meridional) plane. In particular, the narrow linewidth preferentially enhances the horizontal resolution. The difference between the horizontal and vertical resolutions is clearly exhibited by the PSFs shown Figure 4 (a). This large asymmetry in resolution could be corrected for by moving the detector further from the crystal (i.e., closer to the sagittal focus) to achieve a more symmetric PSF. However, during our experimental campaigns, we chose to keep it fixed to enable rapid shot-to-shot comparisons.

Figure 5 (a) and (b) show that the vertical resolution, for the y = 0 position has a minimum of 73 μm at z = 0 mm and then degrades to 112 μm at the top and bottom of the FoV (z = +/-5 mm positions). Similarly, the horizontal resolution varies from 9 to 31 μm. These values do not include the image plate response. While notable, the space-dependent variations in resolution were

not observed in the images likely due to the motion blur caused by the laser propagation and the expansion of the laser-heated gas over the duration of the laser pulse.

Throughput and depth of focus are the two remining parameters to consider in Figure 5. The throughput variation is small and less than 5% relative to the z = 0 position. Unfortunately, the depth of focus is relatively small and similar to the emission size. Using the root-two metric described earlier, the DoF is 0.7 mm in the horizontal plane and 0.5 mm in the vertical plane. The difference is due to the difference in size of the reflecting portions of the mirror ($L_{a,mer}$ and L_{sag}) . At present, it is not clear how this effect is manifested in the images shown in Figure 9, and it is likely obscured by motion blur and the spatially-broad nature of the source. Further ray tracing of extended emission volumes is required to explore this effect. Despite this disadvantage, the Ar-Imager has proven useful and had two notable achievements. It captured the first quasi-monoenergetic x-ray images of the laser-heated gas [9]. And, separately, it enabled a multi-objective analysis that provided a three-dimensional mapping of the electron-temperature within the volume of the laser heated gas [39].

B. Continuum Imaging

It was discovered during the initial fielding of the Ar-Imager that higher-order reflections at energies $n \times 3.1$ keV ($n = 2, 3, \ldots$ etc.) from the Ge (220) crystal could be used to image the continuum emission from the hot plasma generated during the stagnation phase of the implosion. In this imaging mode, the RCA is filled uniformly by a smooth continuum spectrum with no spectral lines present to further enhance the horizontal resolution. Figure 10 (a) shows one of these images obtained from MagLIF shot z2708. The image shows a narrow column of emission with a diameter of roughly 100 μm with a vertical extent of 8 mm. This continuum imaging configuration is called the "Continuum X-Ray Imager", or CXI, and its parameters are listed Table

I. The theoretical resolution, including the image plate resolution, at the center of the FoV is 65 (horizontal) x 82 μm (vertical). The CXI was the primary imaging diagnostic for MagLIF experiments that occurred from July 2015 to November 2017. Additional images can be found in

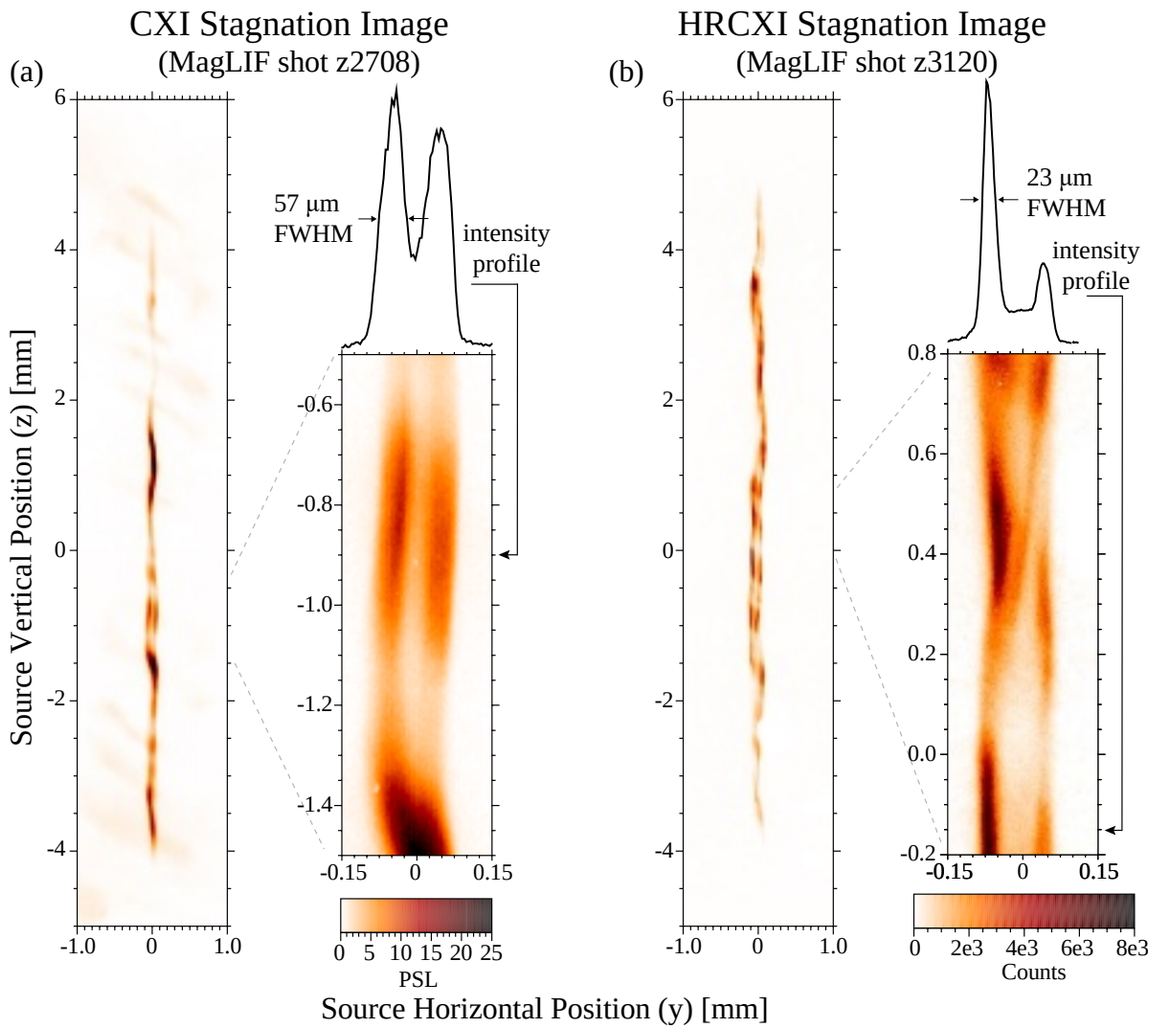

Figure 10. (a) X-ray emission image from a MagLIF stagnation event captured with the spherical crystal imager known as the CXI. The CXI was the first x-ray imaging diagnostic to reveal bifurcations in the column. (b) A higher resolution image of a similar MagLIF experiment captured with an improved version of the CXI known as the HRCXI. In both images, no spatial fiducial was present to indicate the FoV origins of the imager. Therefore, the placement of z = 0 on the images is only approximate and has an uncertainty of ±2 mm, which was estimated by comparing the relative length of the column emission and the initial liner length (10 mm). The placement of y=0 on the images was set to the intensity-weighted, horizontal-center of the column emission.

[8-10, 42]. Despite the relatively coarse resolution, the CXI provided the first images that revealed the radial structure in the column emission.

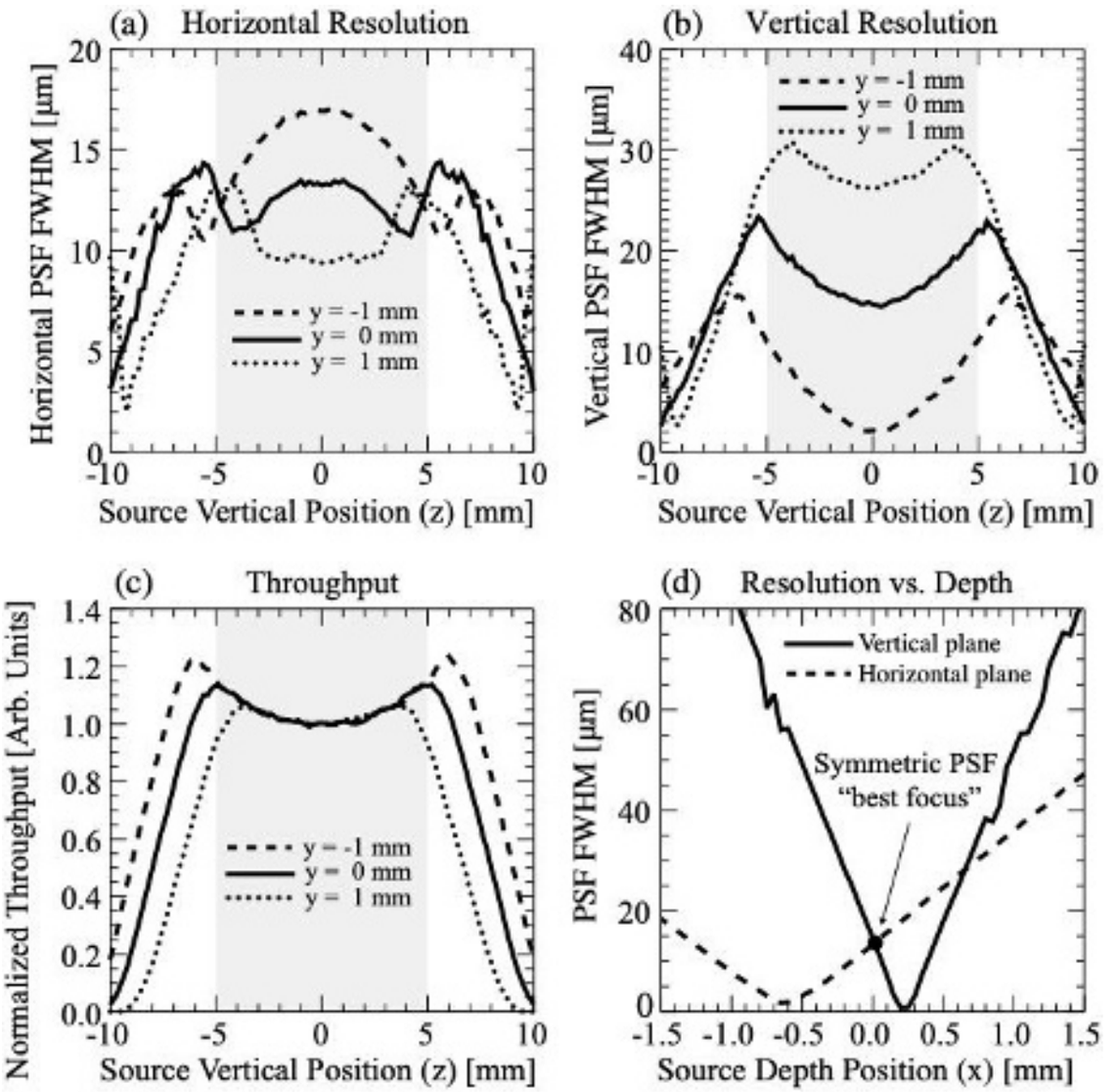

Figure 11. SHADOW3 ray-tracing results for the HRCXI configuration using a point source with E_o = 6213.7 eV. Image plate resolution was not included. (a)(b)(c) Horizontal and vertical resolutions and throughput for different source positions in (y, z)- plane plotted as a function of the z-coordinate (i.e., vertical position) for three horizontal positions: y =-1 ,0, and 1 mm. The throughput was normalized to the z = 0 mm position. The grey shaded regions define the required vertical FoV from z = -5 to 5 mm. (d) Resolution variations for different source positions in source-to-crystal direction (i.e., x-axis or depth position). Source movements toward the crystal are positive values. The HRCXI operates with a symmetric PSF with the source at x=0 as shown in the plot. Coordinate axes are defined in Figure 2.

The initial observation of radial structure in the stagnation column motivated improvements in spatial resolution. This was achieved with the CXI by increasing the Bragg angle to 86° and reducing $L_{a,mer}$ from 7 mm to 3 mm by implementing a narrower RCA. Due to the broadband nature of the continuum emission the choice of Bragg angle (or equivalently E_o)

and bandwidth are not constrained by a particular spectral line. This allowed us to choose a configuration that maximized the Bragg angle, and hence the resolution (see Eq. 7). The higher resolution configuration is called the "High-Resolution Continuum X-ray Imager", or HRCXI, and its parameters are listed in Table I. The theoretical resolution, including IP response, is 15 μm (horizontal) and 16 μm (vertical). Figure 10 (b) shows one of the first images taken with the HRCXI. The experimental image lacks a spatial fiducial, so it is challenging to quantify the resolution and locate the center of the FoV; however, emission features are observed with spatial scales down to ~20 microns, which were not observed in data from the CXI. Additionally, offline tests (see the next section) demonstrated an improvement in resolution over the CXI.

Similar to the Ar-Imager, synthetic grid images of the CXI and HRCXI configurations were produced by ray tracing and are shown in Figure 6 (b) and (c). The grid images clearly demonstrate the improved resolution of the HRCXI. The detailed plots from the HRCXI ray-tracing are shown in Figure 11. We chose not to present the detail plots of the CXI configuration imager since this configuration is no longer in use, but we note that both the CXI and HRCXI maintain a stable resolution and throughput values along the z = +/- 5 mm for a fixed y-location. For the HRCXI, the throughput increases by 15% from z = 0 to z = +/- 5 mm. Looking at Figure 11 (a) and (b), which neglects the image plate resolution, and considering only the y = 0 position, the horizontal resolution varied between 11 and 13 μm and vertical resolution varied between 15 and 22 μm over the z = 0 to z = +/- 5mm positions. These throughput and resolution variations do not appear to have a noticeable effect on the experimental images, yet no systematic study has been performed. Similar to the Ar-Imager, the HRCXI has a small DoF. Neglecting detector resolution and only considering the center ray, the HRCXI has a DoF of 0.1 mm in the sagittal plane, and 0.3 mm in the meridional plane. While this is small and comparable to the width of the

stagnation column, small deviations around the symmetric PSF position (see Figure 11(d)) do not cause a complete defocusing of the image, rather they will produce an asymmetric PSF that will have an enhanced resolution along one axis (e.g., vertical) and a degraded resolution in the opposing axis (e.g., horizontal). The end result is not obvious and further work with synthetic 3D images that include PSF spatial variations is required to understand the impact of a small DoF.

The interpretation of the continuum images is complicated by the existence of multiple crystal reflections, each originating from a different reflection order (i.e., n = 1, 2, or 3 in Eq. 1). Each reflection is superimposed on the others and cannot not be uniquely identified. However, we can estimate the Be attenuation and crystal reflectivity, which modify the relative strengths of the reflections as observed by the detector. The estimated density and thickness of the compressed Be liner are approximately 15 g/cc and 0.5 mm [43]. At these conditions the Be is expected to block the 1st order reflection ($h\nu$ = 3.1 keV, transmission =10^{-4} %), but allow significant transmission of the 2nd order reflection ($h\nu$ = 6.2 keV, transmission =19%), 3rd order reflection ($h\nu$ = 9.4 keV, transmission = 61%), 4th order reflection ($h\nu$ = 12.4 keV, transmission = 77%) and higher orders. Due to the low integrated reflectivity of the 4th and higher-order reflections, and the diminishing brightness of the continuum, we expect the reflected signal from these higher orders to be weak relative to the others. These estimates indicate the signal is almost entirely from the 2nd (6.2 keV) and 3rd order (9.4 keV) reflections assuming the continuum emission is generated by plasma temperatures in the range of 2 to 3 keV

The 1st order reflection is responsible for the large diagonal stripes that appeared in some early MagLIF experiments, which are likely evidence of a helical magneto-Rayleigh instability on the outside of the Be liner [14]. The stripes are visible in Figure 10 (a). These stripes are wider than the column and extend out to a diameter of ~1 mm. Images from a time-gated pinhole camera

revealed the stripes are caused by soft x-ray emission generated on the outside of the liner [9], and so the emission was not filtered by the compressed liner wall. In later experiments, the stripe signal was reduced by adding a 50 μm thick Kapton filter to the detector cassette. The emission intensity of the central column appeared unaffected, further confirming that the stripes were seen with softer x-rays from the 1st order reflection. A 0.5 mm thick polyimide filter is standard for the HRCXI, eliminating nearly all the 1st order contribution.

C. Spatial Resolution Measurements

Spatial resolution measurements are important because the presence of defects in the crystal lattice or form errors in the surface profile of the crystal may cause the optic to deviate from the theoretical resolution. These effects are not accounted for in the ray tracing. Figure 12 (a) shows the experimental configuration used to measure the resolution of the CXI and HRCXI. We used a laser heated, Au foil to generate broad-band x-ray emission, which functioned as an area backlighter for an Au grid. The grid was placed at the object position, and the Au foil was located 1 mm behind the grid. The Au foil consisted of a 2 μm thick, pure Au-coating (purity ~ 99.999%) deposited onto a 50 μm thick polyester backing with a 45 Å thick Ti adhesion layer in between. The grids were obtained from SPI Supplies (model numbers: 2020G-XA and 2040G-XA).

The Z-Beamlet laser provided a 2 kJ (λ = 527 nm) main pulse with a 2 ns duration [44]. The main pulse was typically preceded by a 0.2 kJ pre-pulse that occurred 3.5 ns before the main pulse and had a duration equal to 0.5 ns [45]. A distributed phase plate was used to create a uniform spot with a diameter equal to 565 μm, which contained 75% of the laser energy. Assuming a 70% transmission value for the laser optical chain, this resulted in an irradiance of 2 x 10^{14} W/cm^2 for the main pulse. In some experiments the pre-pulse was not used, and this generated a more

uniform, but dimmer x-ray spot. In either case, there was no evidence for Au L-shell line emission that, if present, would have the potential to affect the horizontal resolution of the 9 keV reflection.

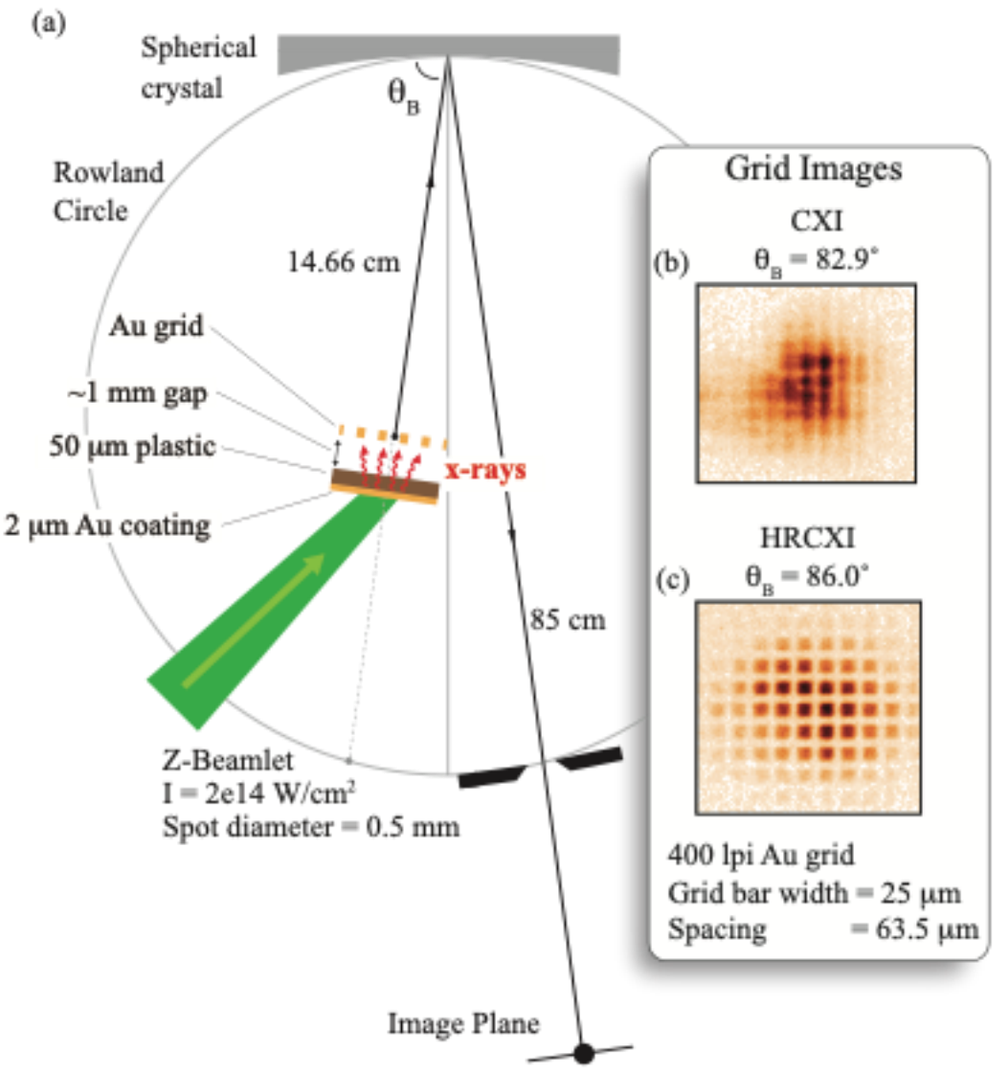

Figure 12. (a) Experimental setup for evaluating the resolution of the spherical crystal imagers known as the CXI and HRCXI. (b) CXI grid image with the grid center located at (x,y,z) = (0,0,0). The grid is clearly not resolved (c) HRCXI grid image with the grid center located at (x, y, z) = (0,0,0). The grid is now fully resolved due to the increase in θ_B.

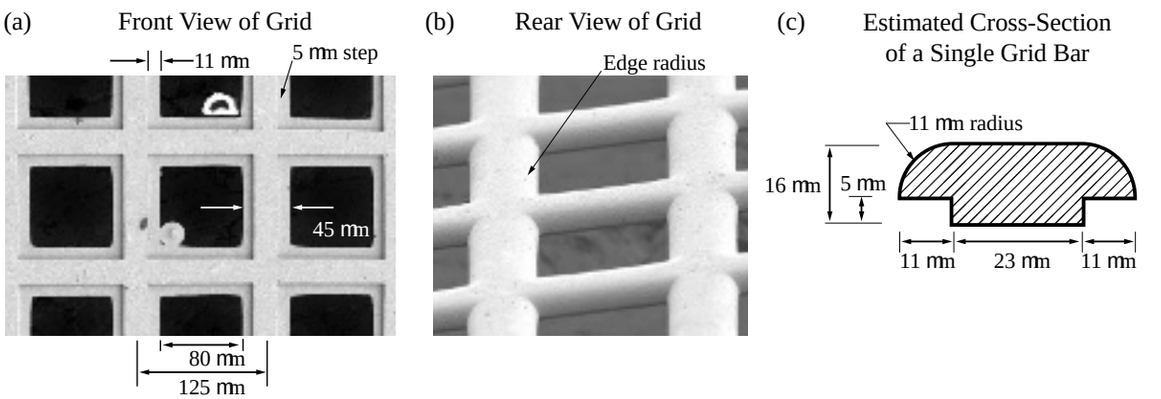

Figure 13. (a) SEM image of the front side of a 200 lpi Au grid showing the 11 μm wide step feature. The circular feature in the center of the image is an artifact from manufacturing. (b) SEM image of the opposing side showing the radius feature on the grid bars. (c) Estimated cross-section model of a single grid bar used to calculate synthetic transmission patterns.

The grid images shown in Figure 12 (b) and (c) demonstrate the improved resolution that resulted from an increase in θ_B. The improvement in resolution was easily seen by eye. However, extracting a resolution value from the CXI image shown Figure 12 (b), and other images with coarser grids (e.g., bar spacing = 250 microns), was not possible because the holes and bars were severely under-resolved. Wider bars and holes that are at least twice the width of the PSF are needed to improve the accuracy of the measurement. For now, we must rely on the ray tracing calculations to assess the resolution of the CXI configuration. Note that these calculations indicated the PSF has a non-Gaussian shape as shown in Figure 4 (b).

For the HRCXI configuration a resolution measurement was possible using the grid images shown in Figure 14 (a) and (b). For these measurements a 200 lpi Au grid (bar spacing = 125 μm) was used to fully resolve the grid hole, which in-turn enabled an accurate reconstruction of the underlying x-ray spot intensity. The measurement procedure begins by sampling the signal in the holes and then spline-fitting a surface to these points in order to create a synthetic x-ray emission spot that has the same intensity values as the data. A grid pattern is then applied to the synthetic

spot by calculating the x-ray transmission of the grid bars. Unfortunately, the grids had a non-uniform thickness profile that resulted from unsharp edges and a thickness step surrounding each hole. These features were measured using a Keyence VK-X3000 3D Surface Profiler and further observed with a scanning electron microscope (SEM). SEM images are shown Figure 13 (a) and (b). Figure 13 (c) presents the cross-section model that approximates the thickness variations and edge radius. The transmitted signal values relied on this model and included the x-ray transmission values for the n = 1, 2, 3, and 4th order reflections (i.e., x-ray energies equal to 3.1, 6.2, 9.3, and 12.4 keV). The relative amounts of each were estimated by applying an energy specific transmission correction to the synthetic grid. These values were informed by the measured x-ray spectrum and weighted by the theoretical throughput values for each reflection order and associated detector filters.

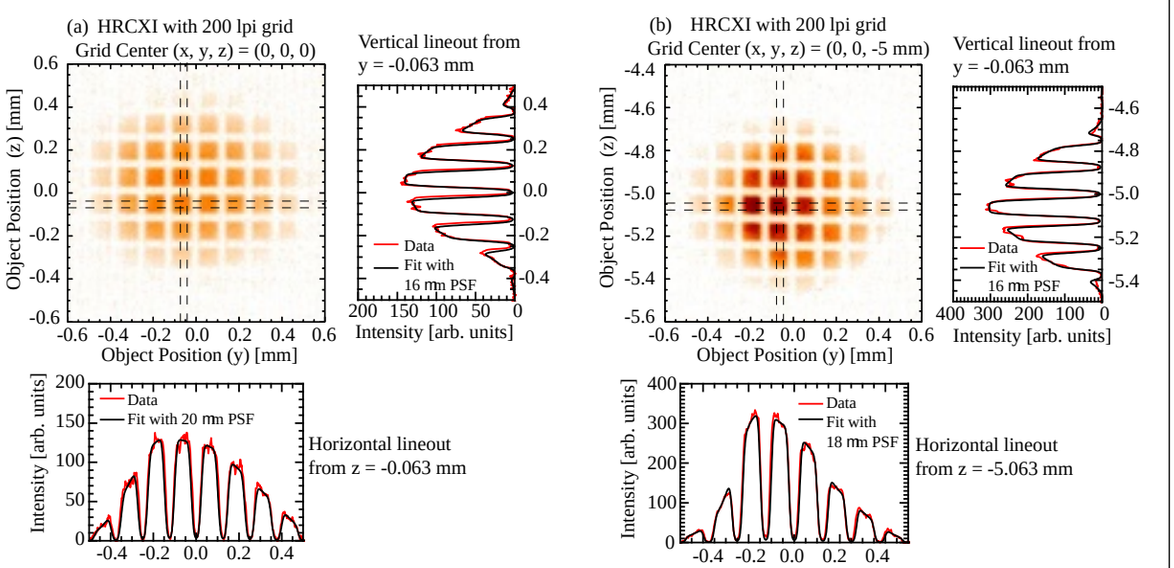

Figure 14. Grid images from the HRCXI using a 200 lpi Au grid (bar width = 45 μm, spacing = 125 μm) were used to estimate the spatial resolution. (a) Center of grid located at (x, y, z) = (0,0,0). Inferred resolution = 20 ± 4 μm (horizontal) x 16 ± 4 μm (vertical). (b) Center of grid located at (x, y, z) = (0, 0, -5mm). Inferred resolution = 18 ± 2 μm (horizontal) x 16 ± 2 μm (vertical). The x-ray spot is brighter here due to the use of a pre-pulse in the laser pulse shape.

The entire synthetic image was then progressively blurred with Gaussian PSF functions, and lineouts were extracted and compared to the data lineouts over a range limited to ± 0.3 mm relative to the grid center. The synthetic lineout that minimized the difference between the synthetic and data lineouts was found, and the measured resolution was then taken as the FHWM of the associated PSF that generated the synthetic image. The best fit PSF included the intrinsic image plate resolution since no attempt was made to deconvolve the image plate resolution from the image or lineouts. The measurement uncertainty is reported as the $\pm 1\sigma$ confidence interval determined by evaluating the goodness of fit between the experimental and synthetic lineouts. We note that the average PSF width increased by 1 to 2 μm if the synthetic images assumed the grid had sharp edges and a uniform thickness.

		HRCXI Theoretical Resolution [μm]	**HRCXI Measured Resolution [μm]**
Grid Position	z = 0 mm	15 (H), 16 (V)	20 ± 4 (H), 16 ± 4 (V)
Grid Position	z = -5 mm	15 (H), 22 (V)	18 ± 2 (H), 16 ± 2 (V)

Table II. Measured and theoretical resolutions for the HRCXI. All resolution values include the blur due to image plate and scanner. The values are given in the format "horizontal (H), vertical (V)" with horizontal and vertical defined by the y and z axes respectively (see Figure 2).

As shown in Figure 14, the resolution of the HRCXI was measured at two locations: z = 0 and z = -5 mm to demonstrate the large vertical FoV. The results are listed in Table II. The slight asymmetry in the theoretical resolution at z = 0 results from the small difference in the magnifications applied to the image. The larger asymmetry of theoretical resolution at z = -5 mm was expected, and this is clearly seen in the PSF arrays shown in Figure 4 (c). On the other hand, the asymmetry of the measured resolution at z = 0 was not expected and was likely due to a

misplacement of the grid from the nominal x = 0 location. For example, displacing the grid by 100 μm towards the crystal causes the horizontal resolution to degrade, and vertical resolution to improve yielding values of 16 μm (H) and 12 μm (V). These are better than the measured resolutions, which were 20 μm (H), 16 μm (V), but with a similar difference between the horizontal and vertical resolution values. At this point we can only speculate as to why some differences remain outside the measurement uncertainty. Future measurements will more precisely control the grid position, in particular the depth position, and measure the DoF by displacing the grid a known distance. Further work must also be done to determine if the backlit grid technique can accurately measure a non-symmetric PSF, as expected for a displaced grid position.

D. Two-Channel Crystal Imaging

The narrow bandwidth properties of the spherical crystal imager can be exploited for identifying x-ray emission from a specific spectral line and hence a specific ion-species. This was done for the laser heated gas, using the Ar-Imager, and now we apply it to the emission generated at stagnation. In this case, however, the continuum emission is bright enough to form an image, and therefore any additional brightness due to the presence of a spectral line will be superimposed on the continuum image making it difficult to discriminate between the continuum and line emission. A method was needed to subtract the continuum contribution from the line emission image.

This motivated the development of a new configuration with two crystals that were fielded side-by-side in the meridional plane. We refer to this imaging diagnostic as a "two-crystal imager". Figure 8 (b) shows a picture of the two-crystal imager installed in the Z-machine, and a corresponding schematic is presented in Figure 15 (a). Each crystal provided an independent imaging channel. One crystal (known as "Channel-2") was tuned to a spectral line of interest, and the other crystal (known as "Channel-1") was tuned to a near-by line-free region of the continuum. The continuum was captured near the line to minimize the difference in emergent continuum

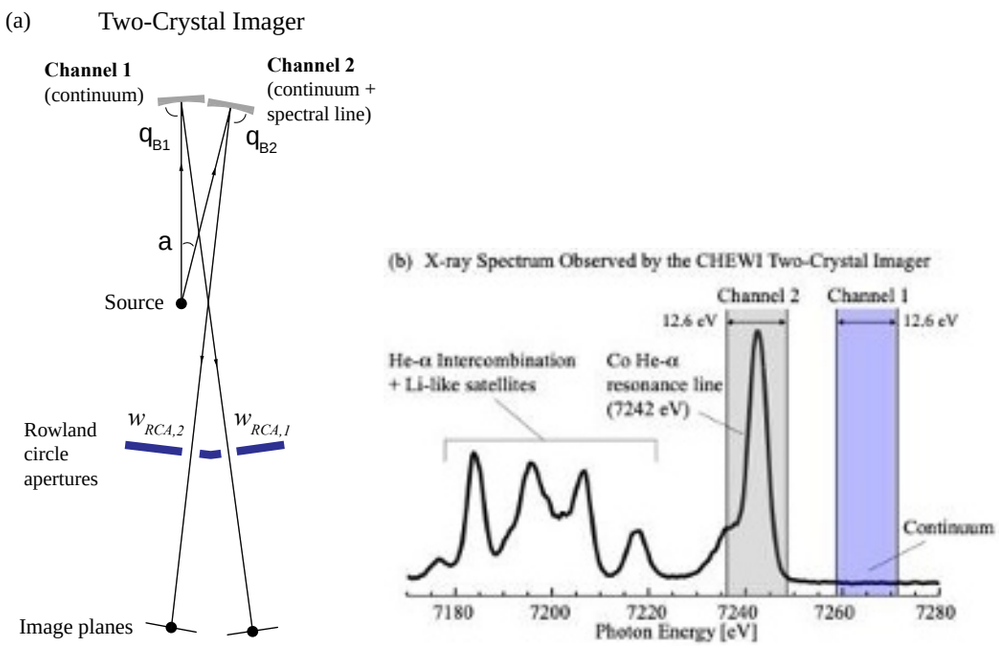

Figure 15. (a) Schematic of the two-crystal imager. The angular separation of the crystals (α) is 5° (b) An example of a measured x-ray spectra from He-like Co emission from MagLIF shot z3078 with the Channel-1 and 2 energy bands overlaid.

intensity observed by each crystal. The continuum contribution present in Channel-2 could then be removed by subtracting Channel-1 from Channel-2 without knowledge of the liner attenuation or source spectrum. A similar technique using toroidal crystals was demonstrated on capsule implosions with Ar and Cl dopants at the GEKKO XII laser facility [13]. Our MagLIF imaging configurations were designed for larger FoVs, which required an RCA, and in some experiments,

included target features that enabled an in-situ method for overlaying and comparing the two images.

Table III lists the parameters of three different, two-crystal imagers that were designed for MagLIF experiments. These imagers capture emission from one of the following spectral lines: Co He-α $^1P_1$ ($h\nu$ = 7242.1 eV), Fe He-β $^1P_1$ ($h\nu$ = 7881.2eV), or Fe Kα_1 ($h\nu$ = 6404.0 eV). The emission from the Fe Kα_1 and Fe He-β $^1P_1$ lines originated from microscopic Fe impurities that are native to the Be grade known as S-65. In other experiments a thin, cobalt coating was applied to the interior of the Be liner or to other internal surfaces [46]. We chose the same crystal plane for each channel in order to minimize the difference in crystal reflectivity and accepted the related difference in Bragg angle ($\Delta\theta_B$= 1.3°) and the resulting difference in spatial resolution. In all cases, the emission from the Fe and Co was monitored with a space-resolving spectrometer known as the XRS^3 [31]. The spectrometer geometry was modified so that a spectral range of 6.3 to 8.1 keV was achieved with a Quartz (20-23) crystal. The high-resolving power ($E/\Delta E \sim 3000$) of the spectrometer enabled a linewidth measurement of the lines observed by the imagers. In addition, the detailed spectrum was used to verify that no unexpected lines contaminated the continuum channel. The space-resolving capability of the spectrometer also identified regions of the column

	Cobalt He-w Imager (CHEWI)		Iron He-β Imager (Iron HEB)		Iron $K\alpha_1$ Imager (Iron KA1)	
	Channel 1	Channel 2	Channel 1	Channel 2	Channel 1	Channel 2
Emission type	Continuum	Co He_α $^1P_1$	Continuum	Fe He-β	Continuum	Fe $K\alpha_1$
Crystal plane	Ge (335)	Ge (335)	Ge (155)	Ge (155)	Quartz (23-50)	Quartz (23-50)
Reflection order	1	1	1	1	1	1
Crystal 2d-spacing [Å]	1.72548	1.72548	1.58437	1.58437	1.95224	1.95224
Center energy, E_o [eV]	7265.0	7242.1	7905.0	7881.2	6425.0	6404.0
Bragg angle, θ_B	81.512°	82.831°	81.865°	83.182°	81.288°	82.614°
Crystal-to-Image distance, s_i [mm]	873.39	862.60	873.39	862.60	873.39	862.60
Magnifications: M_{mer} (horizontal), M_{sag} (vertical)	6.221, 5.957	6.059, 5.883	6.205, 5.957	6.046, 5.883	6.236, 5.960	6.065, 5.882
Spectral Window Width, ΔE_{ap} [eV]	12.6	12.6	12	12	12	12
Rowland circle aperture widths: $w_{RCA,1}$ *and* $w_{RCA,2}$ [mm]	2.876	3.434	2.628	3.161	3.012	3.584
Crystal size (L_{mer} x L_{sag}) [mm]	10x10	10x10	10x10	10x10	10x10	10x10
Meridional FOV [mm][1]	2	2	2	2	2	2
Theoretical Resolution with Image Plate: Horizontal (y) x Vertical (z) [μm][1]	61 x 57	73 x 72	63 x 66	50 x 53	79 x 82	64 x 66
Integrated reflectivity, R_{int} [mrad]	0.128	0.153	0.122	0.146	0.052	0.062
Rocking curve FWHM [mrad]	0.171	0.204	0.200	0.241	0.277	0.334
Active Solid Angle, Ω_{act}, [steradians]	2.14e-5	2.55e-5	2.04e-5	2.43e-5	8.74e-6	1.04e-5

[1]Resolution and FoV were calculated with SHADOW3 using a point source that emits uniformly over the entire spectral window (ΔE_{ap}) set by the RCA. The resolution will improve if the spectral line width is smaller than the spectral window. For the CHEWI configuration, a 4.0 eV FWHM linewidth results in a horizontal resolution of 21 μm. The meridional FOV is defined as the total distance along the horizontal direction (y) over which the full bandwidth is maintained at z = 0 mm. At other z-locations, the meridional FOV may be reduced by vignetting. For bandwidths smaller than ΔE_{ap} the meridional FoV increases.

Table III. This table lists the parameters for three unique two-crystal imaging configurations. For all imagers, the crystal-to-detector distance was 146.62 cm, the crystal radius-of-curvature was 250 mm, and the vertical FoV was 10 mm when the bandwidth is limited by the RCA, and the angular separation (α) of the crystals was 5 °. The detector filters were 50 μm Be and 100 μm Kapton HN film. The R_{int} and rocking curve FWHM were calculated using XOP in the same manner as described in Table I.

where no Co emission was present, and these regions then served as registration points that enabled an accurate overlay of the two images. To date, the utility of the two-crystal imager was best

demonstrated in MagLIF experiments with Co coatings. The remainder of this section will show example data from one such MagLIF experiment.

On Z-shot z3078 a 1 nm thick Co-coating was applied to the bottom half of the interior wall of the Be liner. The two-crystal imager known as CHEWI (Cobalt Helium-w Imager) was fielded in order to image the Co x-ray emission. Channel-2 was centered on the Co He-α resonance line (or "w") at 7242 eV and had a spectral window size equal to 12.6 eV. Channel-1 had the same window size and was centered on the continuum at 7265 eV. The XRS[3] spectrometer showed bright spectra from He-like Co over the lower region of the stagnation column where the coating was initially applied. No Co emission appeared in the upper half of the column. An example of the Co spectrum from this shot is shown in Figure 15 (b). Overlaid on the spectrum are the locations of the Channel-1 and Channel-2 spectral windows. The measured line width for the Co He-α resonance line was 4.0 eV FWHM, which was smaller than the 12.6 eV spectral window set by the RCA. This resulted in an improvement of the horizontal resolution from 61 μm (see Table III) to 21 μm.

Figures 16 (a) and (b) show the raw images from Channel-2 and 1, respectively, and a third image (Figure 16 (c)), which shows the difference image after processing and subtracting Channel-1 from Channel-2. In the Co-free region of the column, which extended from z = 4.5 mm to 9 mm, we assumed that the emerging column emission appeared identical to both channels, and differences in signal intensity and resolution at the image plane were solely due to the Bragg angle difference between the channels. The smaller Bragg angle of Channel-1 produced lower resolutions and decreased crystal reflectivity. The channel-to-channel intensity differences were calculated by comparing the vertical intensity distributions of the Co-free regions. This comparison showed that Channel-2 was on average 1.27 (±0.09) times brighter relative to Channel-1 in the Co-free region, where the uncertainty accounts for the presence of a varying residual signal

after subtraction. The resolution difference was determined by comparing pairs of horizontal lineouts from the same z-coordinate. This showed that the Channel-2 profiles best fit the Channel-1 profiles, on average, after a convolution with a 30 μm FWHM Gaussian. Therefore, the image intensity values from Channel-1 were multiplied by 1.27 and the image was blurred by a 30 μm

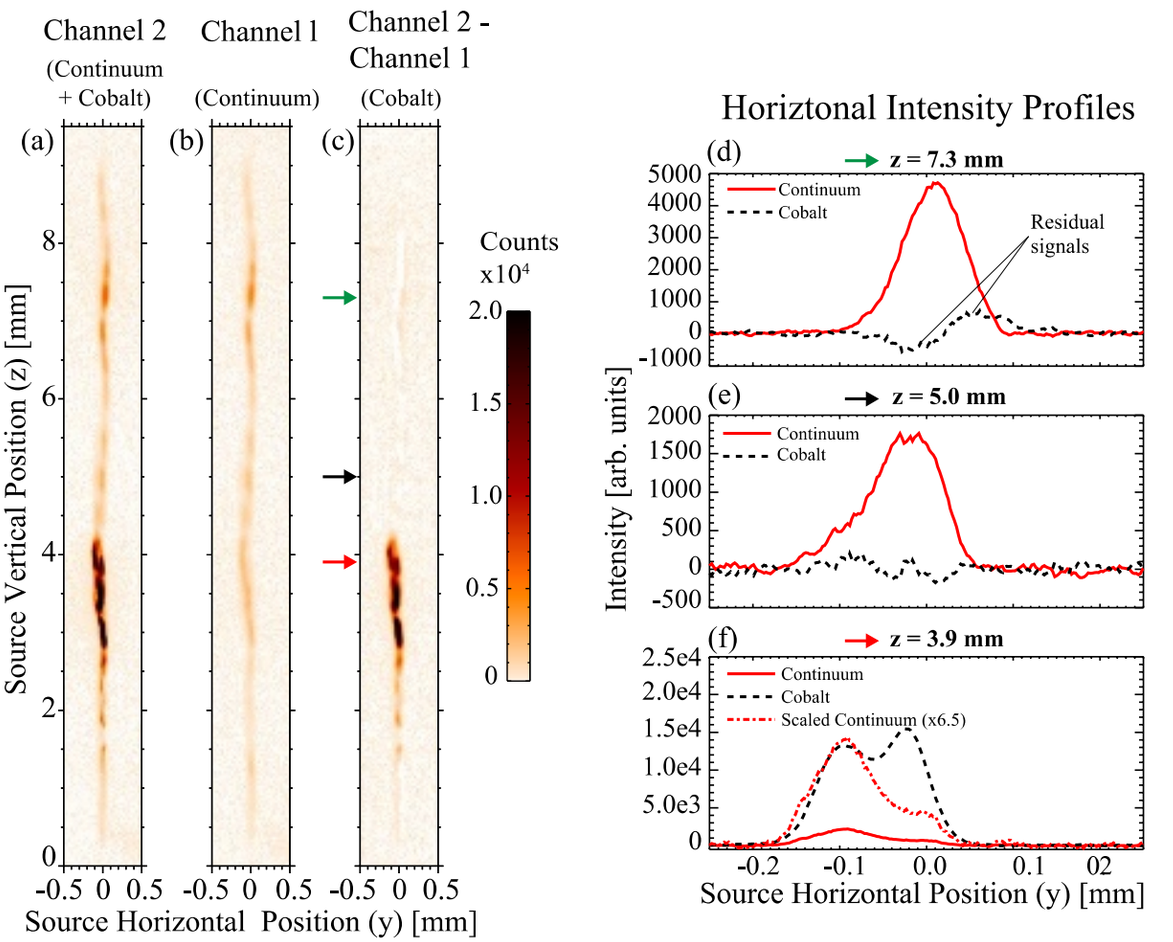

Figure 16. Experimental data from Z-shot z3078 using the two-crystal imager known as CHEWI. (a) Channel 2 image from the CHEWI crystal imager that contains continuum and line emission from the Co He-α resonance line at 7242 eV. (b) Channel 1 image that contains only continuum emission (c) Difference image found by subtracting (b) from (a). The image appears with lower resolution due to the processing necessary for subtraction. A deconvolution could be applied to restore the image to its original resolution. (d)(e)(f) Horizontal intensity profiles from the continuum and cobalt signals at z=7.3 mm, z= 5.0 mm, and z = 3.9 mm. The z=0 position was arbitrarily set near the bottom of the images. The FoV center is near z=5 mm.

FWHM Gaussian. The intensity-weighted, center-of-mass points for a sequence of horizontal lineouts were then used to characterize the orientation of each image. A single translation and

rotation were determined and applied to Channel-1 so that its orientation matched that of Channel-2. Channel-1 was then subtracted from Channel-2 yielding the image shown in Figure 16 (c).

The accuracy of the subtraction was judged by the residual signal that remains in the Co free region after subtraction. Residual signals were expected because there was variation in the 1.27 scaling value. And indeed, looking more closely at individual lineouts, the residual Co feature appears particularly high around z = 7.3 mm (see Figure 16 (d)) and shows an obvious pattern which suggests the presence a systematic error. In contrast, below this region, at z = 5.0 mm (see Figure 16 (e), the residual signal is weaker and more uniform, suggesting a more accurate subtraction was achieved. We are currently investigating the cause of these variations. There are multiple effects to explore including optical distortions, which are slightly different for each channel due to the difference in Bragg angles, and the effects of parallax due to the 5° separation of the crystals.

Fortunately, in this experiment the Co signals were much brighter (6.5x) relative to the continuum, so weak residual features did not affect the comparison of the Co and continuum

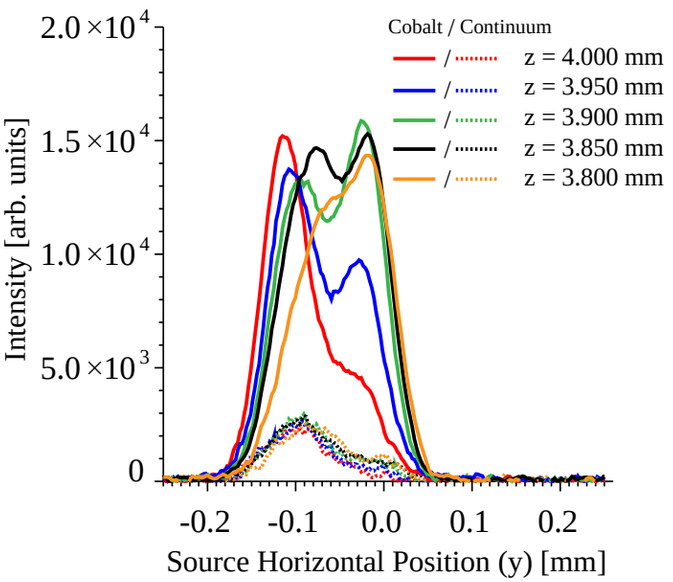

Figure 17. A sequence of horizontal lineouts taken from the images shown in Figure 16 (b) (cobalt) and (c) (continuum). Each lineout is centered on the given z position and averaged over a Δz = 10 μm. The distribution of the cobalt emission changes every 50 μm vertical step, while the continuum distributions remain relatively constant, showing different spatial distributions for the two plasmas.

horizontal intensity profiles. One important example of this is shown in Figure 16 (f), where the Co and continuum horizontal profiles have different shapes. Specifically, the continuum emission decreases toward the y = 0 mm position while the Co emission increases. In addition, Figure 17 shows a vertical sequence of horizontal profiles for the Co and the continuum emission. Over a vertical extent of only 0.2 mm, there are relatively large variations in the Co emission distributions compared to the continuum emission. This is an important result that suggests the Co plasma, which originated from a 1 nm coating on the liner wall, and the plasma that produced the continuum emission can have two different spatial distributions within the stagnated column. Further work is underway to determine the properties of the plasma that generated the continuum emission and that of the plasma surrounding the Co. For the purposes of this paper, these results demonstrate the valuable new insight provided by the two-crystal imager. This compels us to continue fielding the diagnostic and to promote its use in other ICF experiments.

V. Conclusions

In this article we described the operation of a spherical-crystal-based x-ray imaging system that was designed for MagLIF experiments on the Z-machine. We emphasized the importance of the Rowland circle aperture and its ability to maintain a fixed spectral window for all emissions points without limiting the FoV. Several single-optic configurations were designed and implemented for the MagLIF target. The resulting experimental images show an emitting column of plasma that is 6 to 8 mm tall with a characteristic width of 0.1 mm within which finer emission structures exist. This creates unique challenges for an x-ray imaging system that must have a large FoV to capture the entire height and have a high-spatial resolution to resolve the small width of the column. The HRCXI configuration described here was able to successfully meet both requirements, and

provided an average spatial resolution of 18 μm. The HRCXI is now in routine use on the Z-machine.

In addition to the HRCXI, we developed a two-crystal imaging configuration to simultaneously image a spectral line and the near-by continuum emission. This allowed us to generate a difference image that isolated the line emission from the continuum. The technique was described, and an example data set was shown that illustrates the operation and utility of the imager. We believe this represents an important advancement in our ability to visualize liner mix, and more experiments in the future will take advantage of this diagnostic.

Acknowledgements

The authors thank D.B Sinars and J.A. Koch for their encouragement and many enlightening discussions. We would also like to thank the Z and ZBL engineering and operation teams and the General Atomics target fabrication team. This work was supported by Sandia National Laboratories, a multi-mission laboratory managed and operated by the National Technology and Engineering Solutions of Sandia, LLC, a wholly owned subsidiary of Honeywell International, Inc., for the U.S. Department of Energy's National Nuclear Security Administration under Contract No. DE-NA0003525. This article describes objective technical results and analysis. Any subjective views or opinions that might be expressed in the article do not necessarily represent the views of the U.S. Department of Energy or the U.S. Government.

Author Declarations

Conflict of Interest

The authors have no conflicts of interest to disclose.

Data Availability

The supporting data in this article are available from the corresponding authors upon reasonable request except where data is cited in external references.

Bibliography

1. Merrill, F.E., D. Bower, R. Buckles, D.D. Clark, C.R. Danly, O.B. Drury, J.M. Dzenitis, V.E. Fatherley, D.N. Fittinghoff, R. Gallegos, et al., *The neutron imaging diagnostic at NIF (invited).* Review of Scientific Instruments, 2012. **83**(10): p. 10D317.
2. Benedetti, L.R., J.P. Holder, M. Perkins, C.G. Brown, C.S. Anderson, F.V. Allen, R.B. Petre, D. Hargrove, S.M. Glenn, N. Simanovskaia, et al., *Advances in x-ray framing cameras at the National Ignition Facility to improve quantitative precision in x-ray imaging.* Review of Scientific Instruments, 2016. **87**(2): p. 023511.
3. Slutz, S.A., M.C. Herrmann, R.A. Vesey, A.B. Sefkow, D.B. Sinars, D.C. Rovang, K.J. Peterson, and M.E. Cuneo, *Pulsed-power-driven cylindrical liner implosions of laser preheated fuel magnetized with an axial field.* Physics of Plasmas, 2010. **17**(5).
4. Savage, M.E., K.N. Austin, B.T. Hutsel, R.J. Kamm, G.R. Mckee, W.A. Stygar, P.E. Wakeland, N.R. Wemple, and W.M. White, *Pulsed power performance of the Z machine: ten years after the upgrade.* 2017 Ieee 21st International Conference on Pulsed Power (Ppc), 2017.
5. Rovang, D.C., D.C. Lamppa, M.E. Cuneo, A.C. Owen, J. McKenney, D.W. Johnson, S. Radovich, R.J. Kaye, R.D. McBride, C.S. Alexander, et al., *Pulsed-coil magnet systems for applying uniform 10–30 T fields to centimeter-scale targets on Sandia's Z facility.* Review of Scientific Instruments, 2014. **85**(12): p. 124701.
6. Geissel, M., A.J. Harvey-Thompson, T.J. Awe, D.E. Bliss, M.E. Glinsky, M.R. Gomez, E. Harding, S.B. Hansen, C. Jennings, M.W. Kimmel, et al., *Minimizing scatter-losses during pre-heat for magneto-inertial fusion targets.* Physics of Plasmas, 2018. **25**(2).
7. Harvey-Thompson, A.J., M. Geissel, C.A. Jennings, M.R. Weis, M.R. Gomez, J.R. Fein, D.J. Ampleford, G.A. Chandler, M.E. Glinsky, K.D. Hahn, et al., *Constraining preheat energy deposition in MagLIF experiments with multi-frame shadowgraphy.* Physics of Plasmas, 2019. **26**(3).
8. Gomez, M.R., S.A. Slutz, C.A. Jennings, D.J. Ampleford, M.R. Weis, C.E. Myers, D.A. Yager-Elorriaga, K.D. Hahn, S.B. Hansen, E.C. Harding, et al., *Performance Scaling in Magnetized Liner Inertial Fusion Experiments.* Physical Review Letters, 2020. **125**(15).
9. Gomez, M.R., S.A. Slutz, A.B. Sefkow, K.D. Hahn, S.B. Hansen, P.F. Knapp, P.F. Schmit, C.L. Ruiz, D.B. Sinars, E.C. Harding, et al., *Demonstration of thermonuclear conditions in magnetized liner inertial fusion experiments.* Physics of Plasmas, 2015. **22**(5).
10. Gomez, M.R., S.A. Slutz, P.F. Knapp, K.D. Hahn, M.R. Weis, E.C. Harding, M. Geissel, J.R. Fein, M.E. Glinsky, S.B. Hansen, et al., *Assessing Stagnation Conditions and*

Identifying Trends in Magnetized Liner Inertial Fusion. Ieee Transactions on Plasma Science, 2019. **47**(5): p. 2081-2101.

11. Craxton, R.S., K.S. Anderson, T.R. Boehly, V.N. Goncharov, D.R. Harding, J.P. Knauer, R.L. McCrory, P.W. McKenty, D.D. Meyerhofer, J.F. Myatt, et al., *Direct-drive inertial confinement fusion: A review.* Physics of Plasmas, 2015. **22**(11).
12. Kline, J.L., S.H. Batha, L.R. Benedetti, D. Bennett, S. Bhandarkar, L.F.B. Hopkins, J. Biener, M.M. Biener, R. Bionta, E. Bond, et al., *Progress of indirect drive inertial confinement fusion in the United States.* Nuclear Fusion, 2019. **59**(11).
13. Vollbrecht, M., I. Uschmann, E. Förster, K. Fujita, Y. Ochi, H. Nishimura, and K. Mima, *Five channel X-ray imaging of laser fusion plasmas.* Journal of Quantitative Spectroscopy and Radiative Transfer, 1997. **58**(4): p. 965-974.
14. Awe, T.J., R.D. McBride, C.A. Jennings, D.C. Lamppa, M.R. Martin, D.C. Rovang, S.A. Slutz, M.E. Cuneo, A.C. Owen, D.B. Sinars, et al., *Observations of Modified Three-Dimensional Instability Structure for Imploding z-Pinch Liners that are Premagnetized with an Axial Field.* Physical Review Letters, 2013. **111**(23).
15. McBride, R.D., S.A. Slutz, C.A. Jennings, D.B. Sinars, M.E. Cuneo, M.C. Herrmann, R.W. Lemke, M.R. Martin, R.A. Vesey, K.J. Peterson, et al., *Penetrating Radiography of Imploding and Stagnating Beryllium Liners on the Z Accelerator.* Physical Review Letters, 2012. **109**(13).
16. Pikuz, S.A., T.A. Shelkovenko, V.M. Romanova, D.A. Hammer, A.Y. Faenov, V.A. Dyakin, and T.A. Pikuz, *High-luminosity monochromatic x-ray backlighting using an incoherent plasma source to study extremely dense plasmas (invited).* Review of Scientific Instruments, 1997. **68**(1): p. 740-744.
17. Sinars, D.B., G.R. Bennett, D.F. Wenger, M.E. Cuneo, and J.L. Porter, *Evaluation of bent-crystal x-ray backlighting and microscopy techniques for the Sandia Z machine.* Applied Optics, 2003. **42**(19): p. 4059-4071.
18. Aglitskiy, Y., T. Lehecka, S. Obenschain, S. Bodner, C. Pawley, K. Gerber, J. Sethian, C.M. Brown, J. Seely, U. Feldman, et al., *High-resolution monochromatic x-ray imaging system based on spherically bent crystals.* Applied Optics, 1998. **37**(22): p. 5253-5261.
19. Belyaev, L.M., A.B. Gil'varg, Y.A. Mikhaĭlov, S.A. Pikuz, G.V. Sklizkov, A.Y. Faenov, and S.I. Fedotov, *X-ray photography of laser plasmas with the aid of analyzer crystals bent to form second-order surfaces.* Soviet Journal of Quantum Electronics, 1976. **6**(9): p. 1121-1122.
20. Koch, J.A., Y. Aglitskiy, C. Brown, T. Cowan, R. Freeman, S. Hatchett, G. Holland, M. Key, A. MacKinnon, and J. Seely, *4.5-and 8-keV emission and absorption x-ray imaging using spherically bent quartz 203 and 211 crystals.* Review of Scientific Instruments, 2003. **74**(3).
21. Sawada, H., T. Daykin, H.S. McLean, H. Chen, P.K. Patel, Y. Ping, and F. Pérez, *Two-color monochromatic x-ray imaging with a single short-pulse laser.* Review of Scientific Instruments, 2017. **88**(6): p. 063502.
22. Akli, K.U., M.H. Key, H.K. Chung, S.B. Hansen, R.R. Freeman, M.H. Chen, G. Gregori, S. Hatchett, D. Hey, N. Izumi, et al., *Temperature sensitivity of Cu Kα imaging efficiency using a spherical Bragg reflecting crystal.* Physics of Plasmas, 2007. **14**(2): p. 023102.
23. Koch, J.A., O.L. Landen, T.W. Barbee, P. Celliers, L.B. Da Silva, S.G. Glendinning, B.A. Hammel, D.H. Kalantar, C. Brown, J. Seely, et al., *High-energy x-ray microscopy*

techniques for laser-fusion plasma research at the National Ignition Facility. Applied Optics, 1998. **37**(10): p. 1784-1795.

24. Uschmann, I., K. Fujita, I. Niki, R. Butzbach, H. Nishimura, J. Funakura, M. Nakai, E. Förster, and K. Mima, *Time-resolved ten-channel monochromatic imaging of inertial confinement fusion plasmas.* Applied Optics, 2000. **39**(31): p. 5865-5871.
25. Pickworth, L.A., J. Ayers, P. Bell, N.F. Brejnholt, J.G. Buscho, D. Bradley, T. Decker, S. Hau-Riege, J. Kilkenny, T. McCarville, et al., *The National Ignition Facility modular Kirkpatrick-Baez microscope.* Review of Scientific Instruments, 2016. **87**(11): p. 11E316.
26. Marshall, F.J., *Compact Kirkpatrick–Baez microscope mirrors for imaging laser-plasma x-ray emission.* Review of Scientific Instruments, 2012. **83**(10): p. 10E518.
27. Bachmann, B., T. Hilsabeck, J. Field, N. Masters, C. Reed, T. Pardini, J.R. Rygg, N. Alexander, L.R. Benedetti, T. Döppner, et al., *Resolving hot spot microstructure using x-ray penumbral imaging (invited).* Review of Scientific Instruments, 2016. **87**(11): p. 11E201.
28. Do, A., L.A. Pickworth, B.J. Kozioziemski, A.M. Angulo, G.N. Hall, S.R. Nagel, D.K. Bradley, T. McCarville, and J.M. Ayers, *Fresnel zone plate development for x-ray radiography of hydrodynamic instabilities at the National Ignition Facility.* Applied Optics, 2020. **59**(34): p. 10777-10785.
29. Thorne, A.P., *Spectrophysics*. Second ed. 1988: Chapman and Hall Ltd. 390.
30. Stoeckl, C., T. Filkins, R. Jungquist, C. Mileham, N.R. Pereira, S.P. Regan, M.J. ShoupIII, and W. Theobald, *Characterization of shaped Bragg crystal assemblies for narrowband x-ray imaging.* Review of Scientific Instruments, 2018. **89**(10): p. 10G124.
31. Harding, E.C., T. Ao, J.E. Bailey, G. Loisel, D.B. Sinars, M. Geissel, G.A. Rochau, and I.C. Smith, *Analysis and implementation of a space resolving spherical crystal spectrometer for x-ray Thomson scattering experiments.* Review of Scientific Instruments, 2015. **86**(4).
32. Förster, E., R.J. Hutcheon, O. Renner, I. Uschmann, M. Vollbrecht, M. Nantel, A. Klisnick, and P. Jaeglé, *High-resolution x-ray imaging of extended lasing plasmas.* Applied Optics, 1997. **36**(4): p. 831-840.
33. Koch, J.A., J.E. Field, J.D. Kilkenny, E. Harding, G.A. Rochaud, A.M. Covington, E.C. Dutra, R.R. Freeman, G.N. Hall, M.J. Haugh, et al., *X-ray Doppler Velocimetry: An imaging diagnostic of 3D fluid flow in turbulent plasma.* High Energy Density Physics, 2017. **23**: p. 184-187.
34. Schollmeier, M.S., M. Geissel, J.E. Shores, I.C. Smith, and J.L. Porter, *Performance of bent-crystal x-ray microscopes for high energy density physics research.* Applied Optics, 2015. **54**(16): p. 5147-5161.
35. del Rio, M.S., N. Canestrari, F. Jiang, and F. Cerrina, *SHADOW3: a new version of the synchrotron X-ray optics modelling package.* Journal of Synchrotron Radiation, 2011. **18**: p. 708-716.
36. Ao, T., E.C. Harding, J.E. Bailey, G. Loisel, S. Patel, D.B. Sinars, L.P. Mix, and D.F. Wenger, *Relative x-ray collection efficiency, spatial resolution, and spectral resolution of spherically-bent quartz, mica, germanium, and pyrolytic graphite crystals.* Journal of Quantitative Spectroscopy & Radiative Transfer, 2014. **144**: p. 92-107.
37. Dunham, G., E.C. Harding, G.P. Loisel, P.W. Lake, and L.B. Nielsen-Weber, *Cross-calibration of Fuji TR image plate and RAR 2492 x-ray film to determine the response of*

a DITABIS Super Micron image plate scanner. Review of Scientific Instruments, 2016. **87**(11).

38. Carpenter, K.R., R.C. Mancini, E.C. Harding, A.J. Harvey-Thompson, M. Geissel, M.R. Weis, S.B. Hansen, K.J. Peterson, and G.A. Rochau, *Temperature distributions and gradients in laser-heated plasmas relevant to magnetized liner inertial fusion.* Physical Review E, 2020. **102**(2).
39. Carpenter, K.R., R.C. Mancini, E.C. Harding, A.J. Harvey-Thompson, M. Geissel, M.R. Weis, S.B. Hansen, K.J. Peterson, and G.A. Rochau, *Magnetic field impact on the laser heating in MagLIF*. Physics of Plasmas, 2020. **27**(5).
40. Awe, T.J., K.P. Shelton, A.B. Sefkow, D.C. Lamppa, J.L. Baker, D.C. Rovang, and G.K. Robertson, *Development of a cryogenically cooled platform for the Magnetized Liner Inertial Fusion (MagLIF) Program.* Review of Scientific Instruments, 2017. **88**(9).
41. Bennett, G.R., D.B. Sinars, D.F. Wenger, M.E. Cuneo, R.G. Adams, W.J. Barnard, D.E. Beutler, R.A. Burr, D.V. Campbell, L.D. Claus, et al., *High-brightness, high-spatial-resolution, 6.151 keV x-ray imaging of inertial confinement fusion capsule implosion and complex hydrodynamics experiments on Sandia's Z accelerator (invited).* Review of Scientific Instruments, 2006. **77**(10).
42. Knapp, P.F., M.R. Gomez, S.B. Hansen, M.E. Glinsky, C.A. Jennings, S.A. Slutz, E.C. Harding, K.D. Hahn, M.R. Weis, M. Evans, et al., *Origins and effects of mix on magnetized liner inertial fusion target performance.* Physics of Plasmas, 2019. **26**(1).
43. Hansen, S.B., E.C. Harding, P.F. Knapp, M.R. Gomez, T. Nagayama, and J.E. Bailey, *Changes in the electronic structure of highly compressed iron revealed by X-ray fluorescence lines and absorption edges.* High Energy Density Physics, 2017. **24**: p. 39-43.
44. Rambo, P., J. Schwarz, M. Schollmeier, M. Geissel, I. Smith, M. Kimmel, C. Speas, J. Shores, D. Armstrong, J. Bellum, et al., *Sandia's Z-Backlighter Laser Facility*. SPIE Laser Damage. Vol. 10014. 2016: SPIE.
45. Sinars, D.B., G.R. Bennett, M.C. Herrmann, I.C. Smith, C.S. Speas, L.E. Ruggles, and J.L. Porter, *Enhancement of x-ray yield from the Z-Beamlet laser for monochromatic backlighting by using a prepulse.* Review of Scientific Instruments, 2006. **77**(10): p. 3.
46. Harvey-Thompson, A.J., M.R. Weis, E.C. Harding, M. Geissel, D.J. Ampleford, G.A. Chandler, J.R. Fein, M.E. Glinsky, M.R. Gomez, K.D. Hahn, et al., *Diagnosing and mitigating laser preheat induced mix in MagLIF*. Physics of Plasmas, 2018. **25**(11).

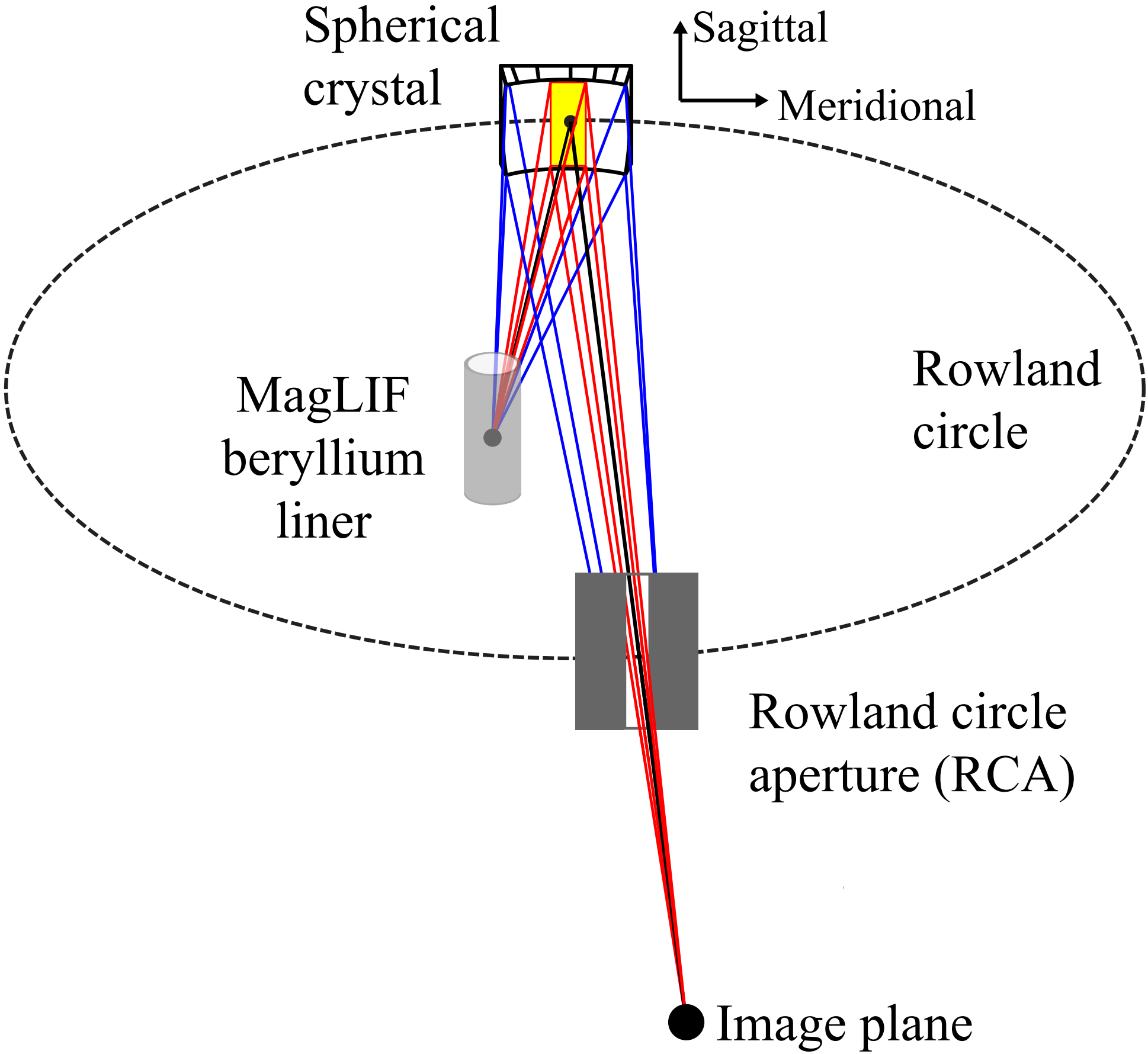
Spherical
crystal
Sagittal
Meridional
MagLIF
beryllium
liner
Rowland
circle
Rowland circle
aperture (RCA)
Image plane

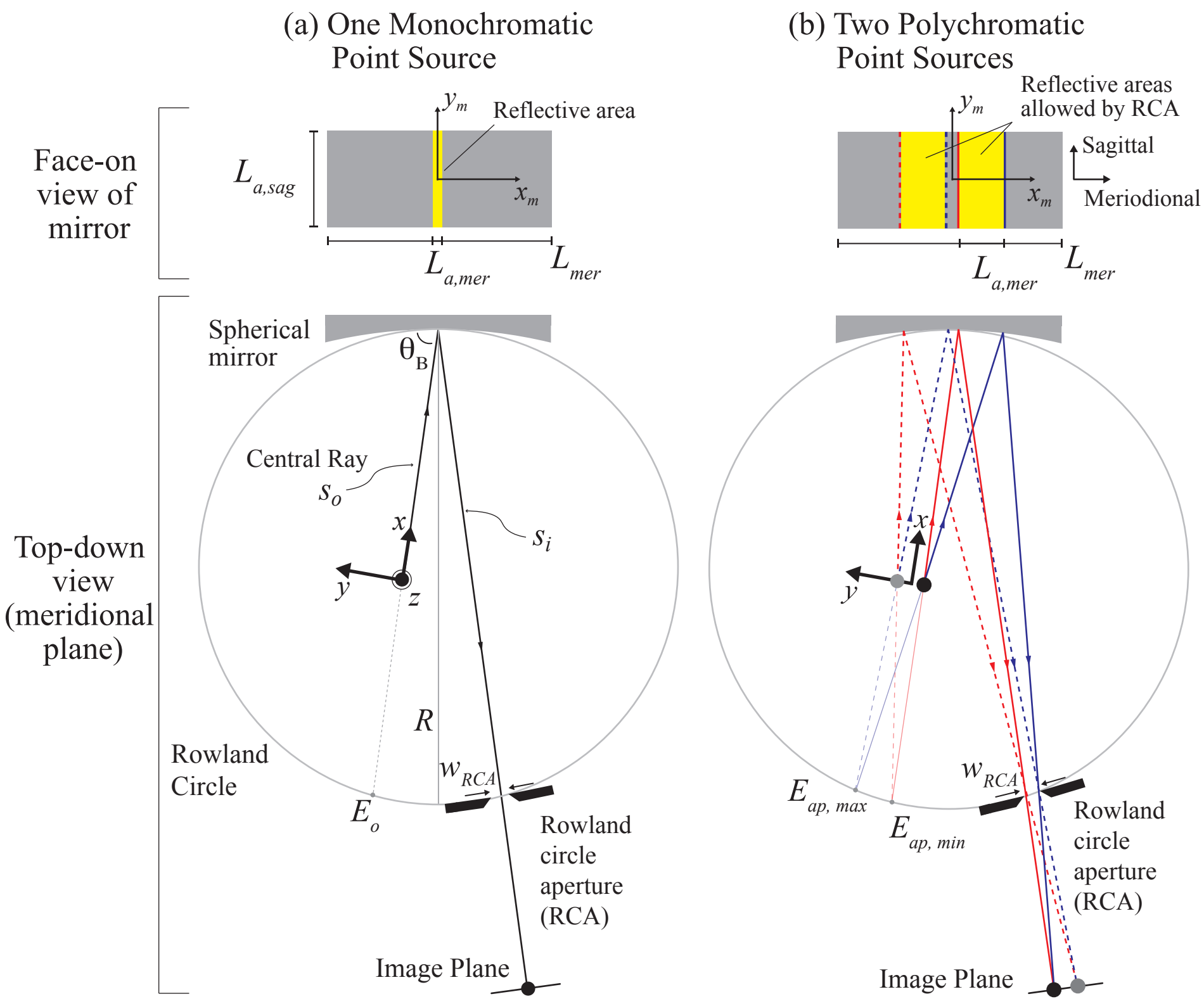
(a) One Monochromatic Point Source
(b) Two Polychromatic Point Sources
Face-on view of mirror
Top-down view (meridional plane)
Reflective area
Reflective areas allowed by RCA
Sagittal
Meriodional
Spherical mirror
Central Ray
Rowland Circle
Rowland circle aperture (RCA)
Image Plane

Reflective Area allowed by the RCA as a Function of Source Position for the HRCXI configuration

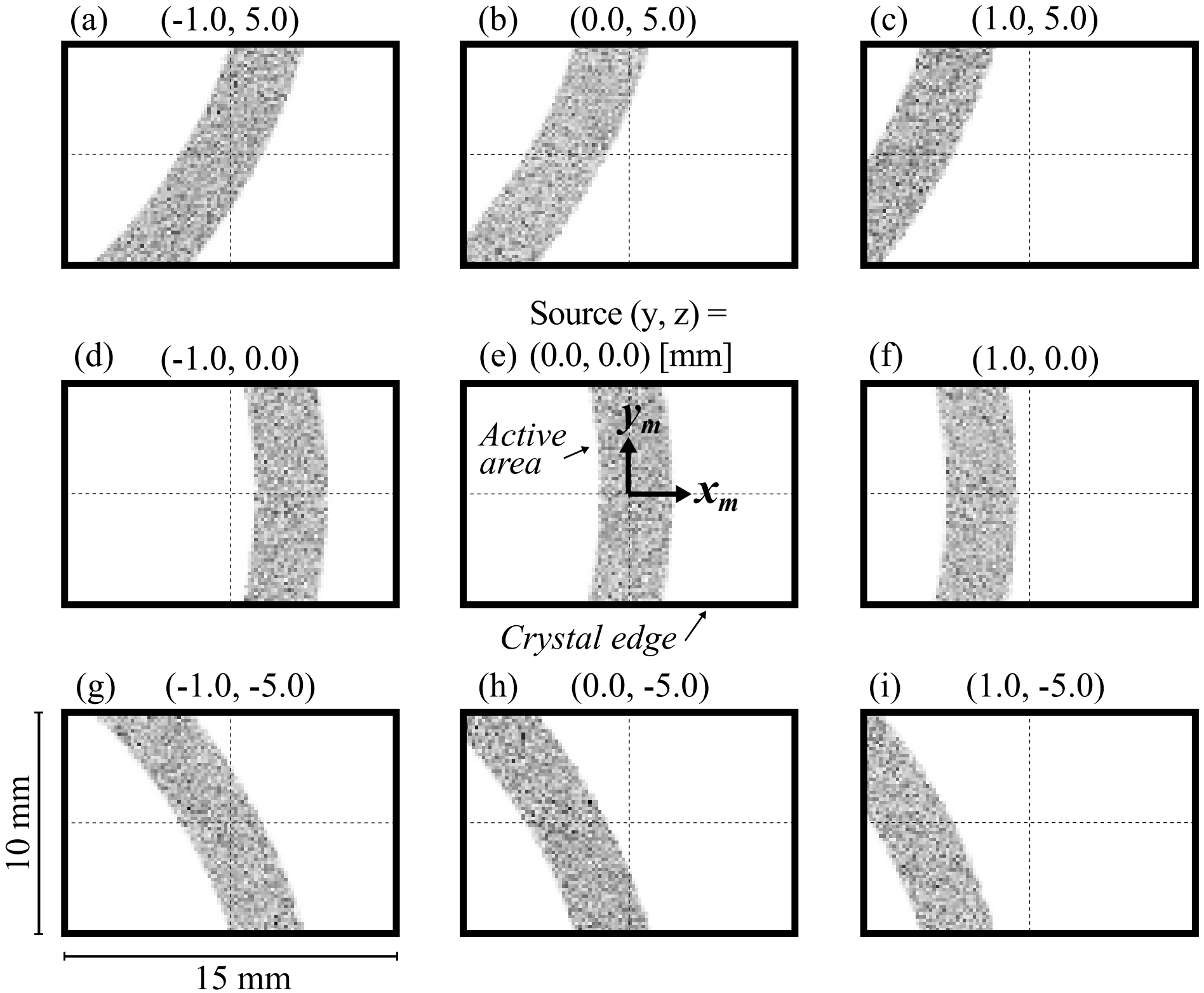

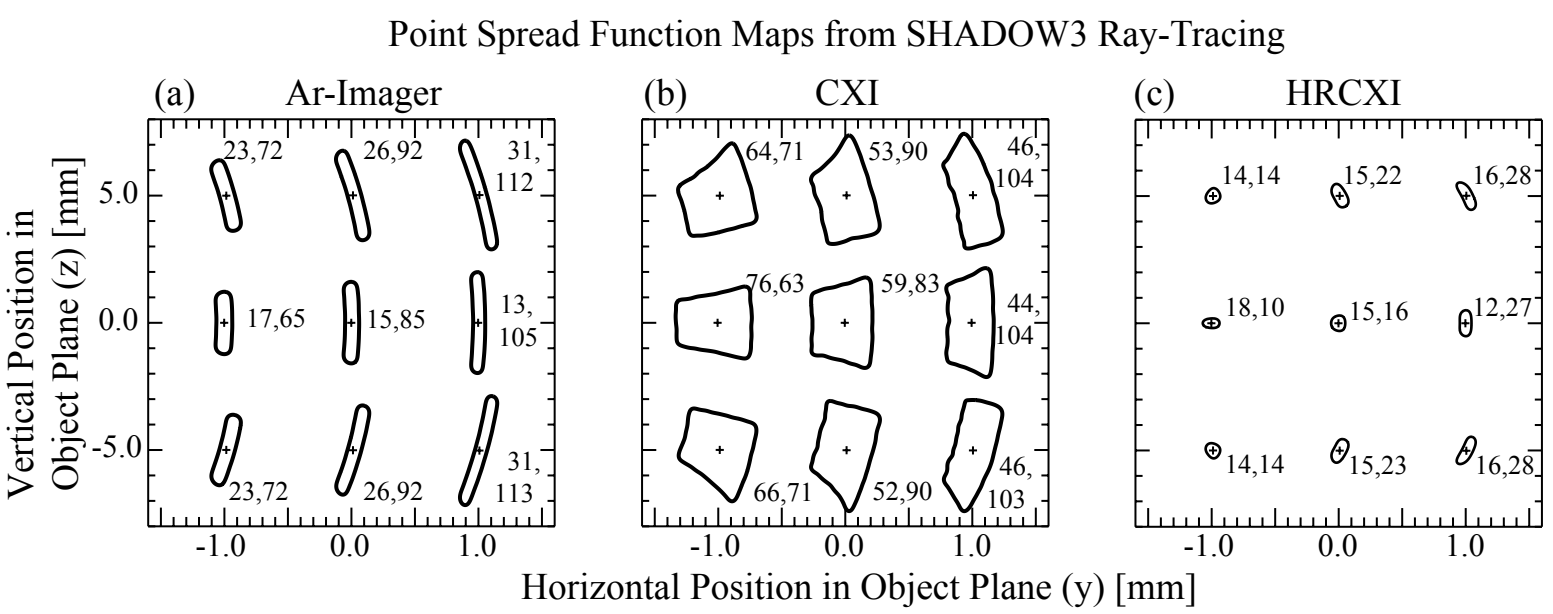
Point Spread Function Maps from SHADOW3 Ray-Tracing
(a) Ar-Imager
(b) CXI
(c) HRCXI
Vertical Position in Object Plane (z) [mm]
Horizontal Position in Object Plane (y) [mm]
5.0
0.0
-5.0
-1.0
0.0
1.0
23,72
26,92
31, 112
17,65
15,85
13, 105
23,72
26,92
31, 113
64,71
53,90
46, 104
76,63
59,83
44, 104
66,71
52,90
46, 103
14,14
15,22
16,28
18,10
15,16
12,27
14,14
15,23
16,28

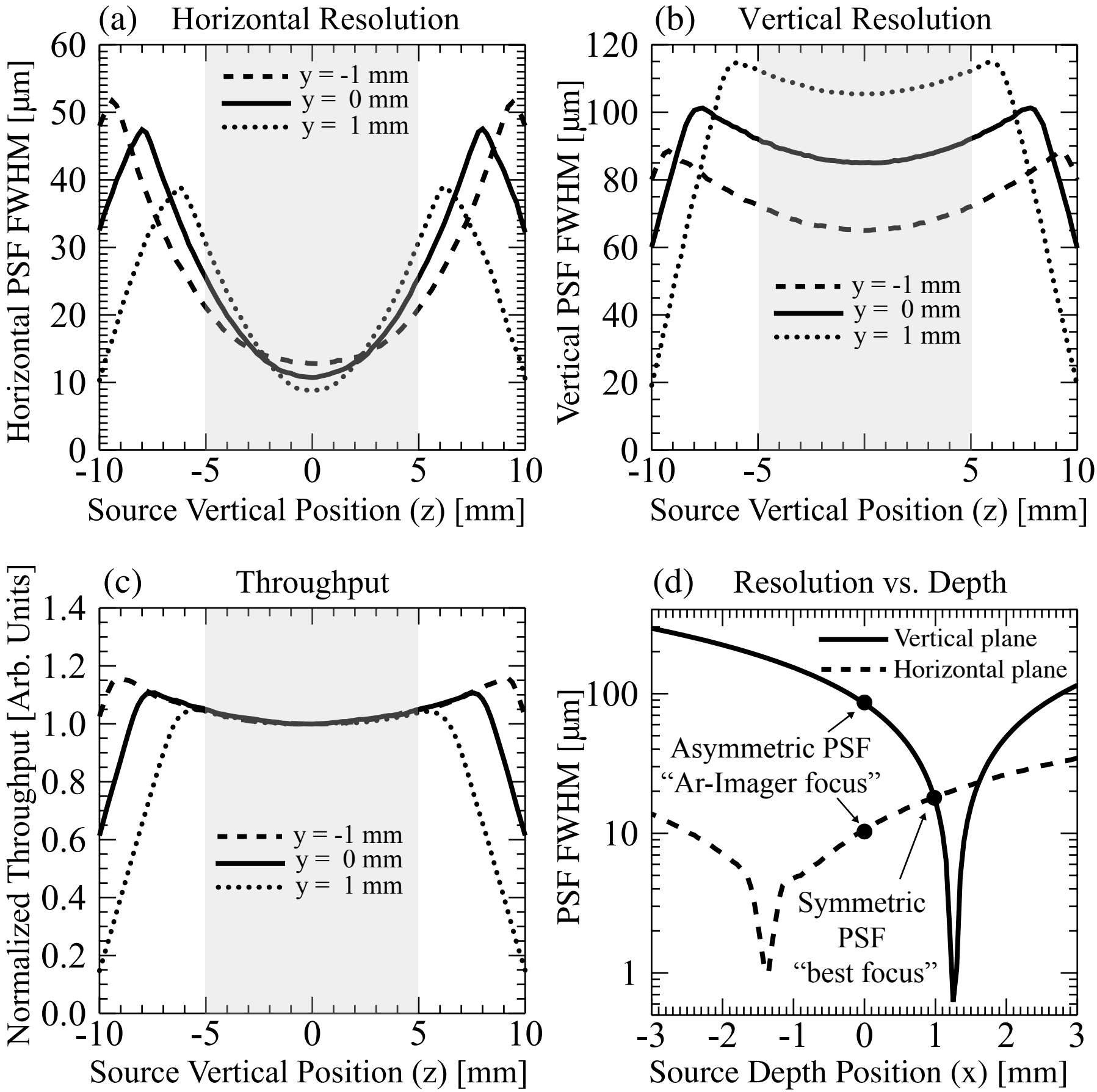
(a) Horizontal Resolution
Horizontal PSF FWHM [μm]
Source Vertical Position (z) [mm]
y = -1 mm
y = 0 mm
y = 1 mm
(b) Vertical Resolution
Vertical PSF FWHM [μm]
Source Vertical Position (z) [mm]
y = -1 mm
y = 0 mm
y = 1 mm
(c) Throughput
Normalized Throughput [Arb. Units]
Source Vertical Position (z) [mm]
y = -1 mm
y = 0 mm
y = 1 mm
(d) Resolution vs. Depth
PSF FWHM [μm]
Source Depth Position (x) [mm]
Vertical plane
Horizontal plane
Asymmetric PSF
"Ar-Imager focus"
Symmetric
PSF
"best focus"

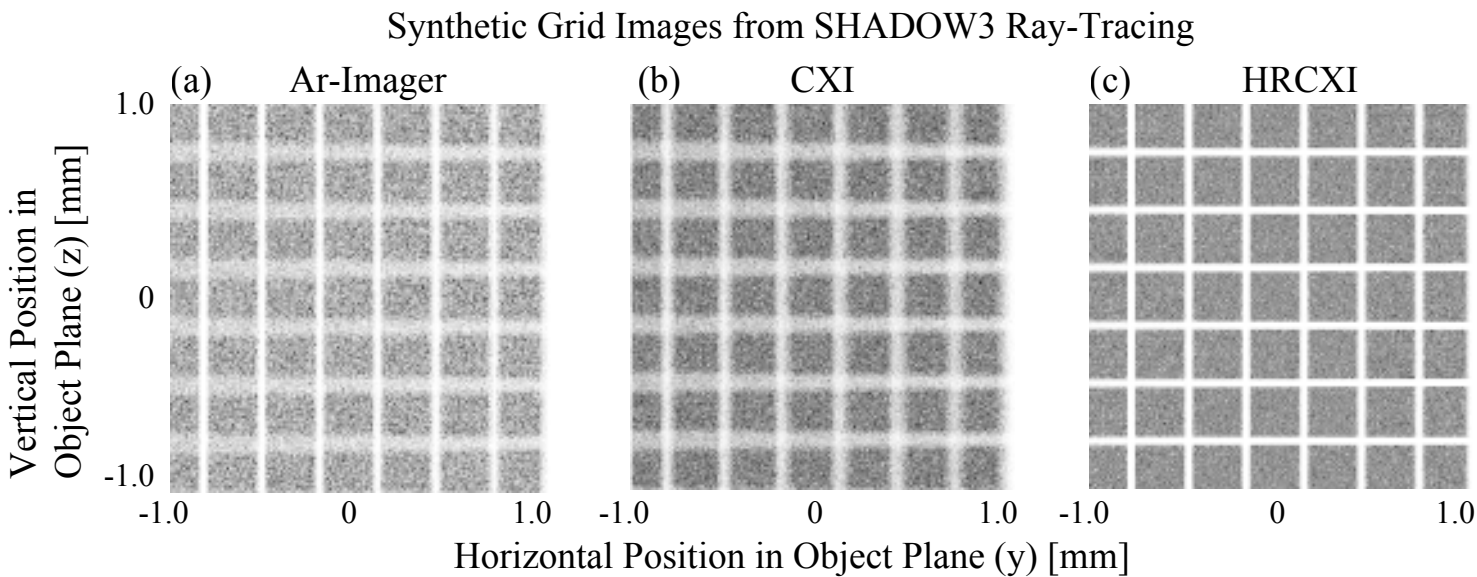
Synthetic Grid Images from SHADOW3 Ray-Tracing
(a) Ar-Imager
(b) CXI
(c) HRCXI
Vertical Position in Object Plane (z) [mm]
1.0
0
-1.0
-1.0
0
1.0
Horizontal Position in Object Plane (y) [mm]

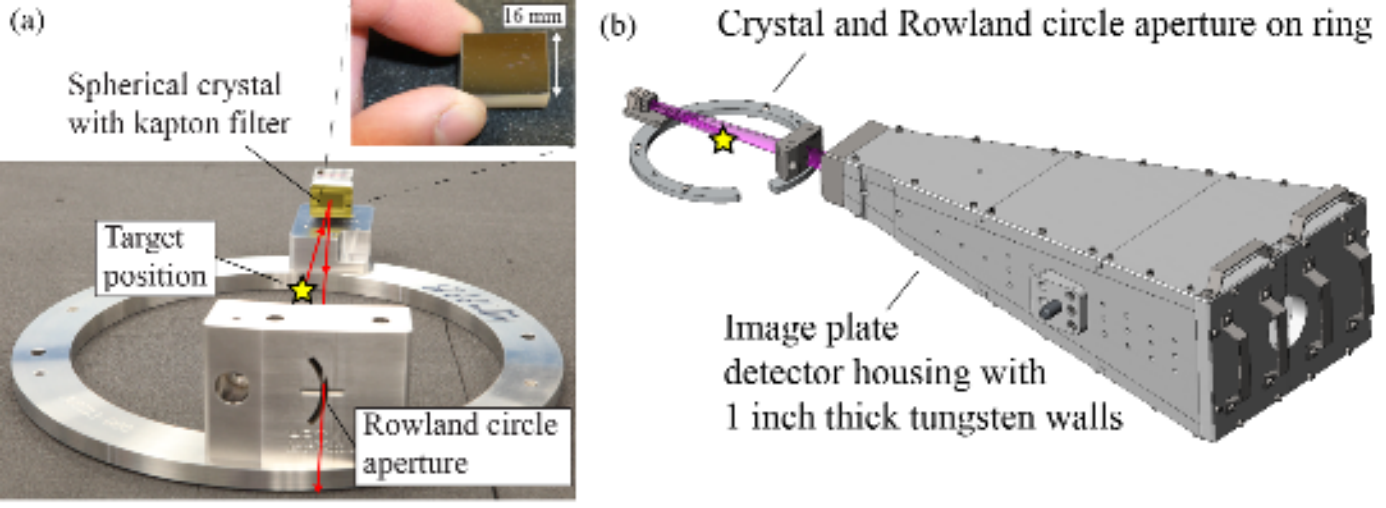
(a)
16 mm
Spherical crystal
with kapton filter
Target
position
Rowland circle
aperture
(b)
Crystal and Rowland circle aperture on ring
Image plate
detector housing with
1 inch thick tungsten walls

(a) HRCXI configuration installed in the Z-machine

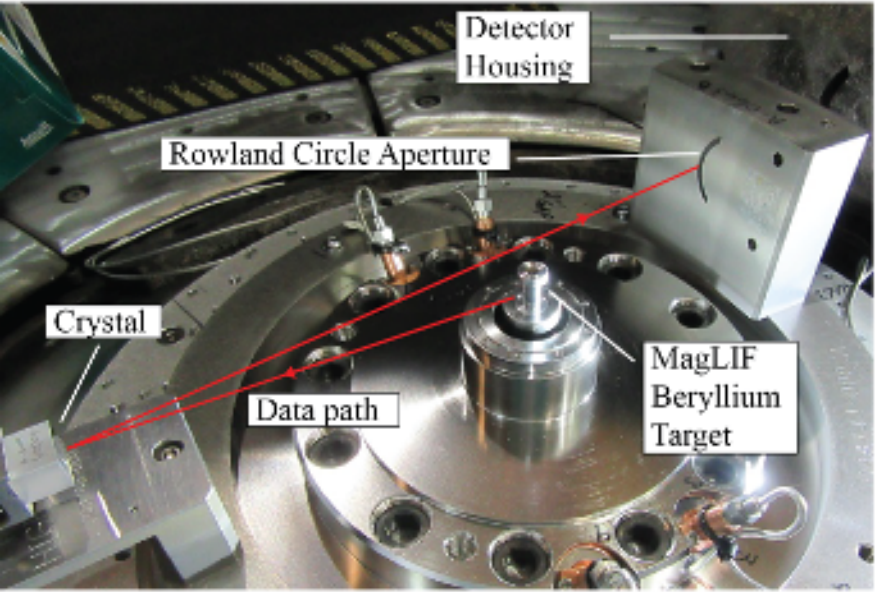

(b) Two-crystal configuration installed in the Z-machine

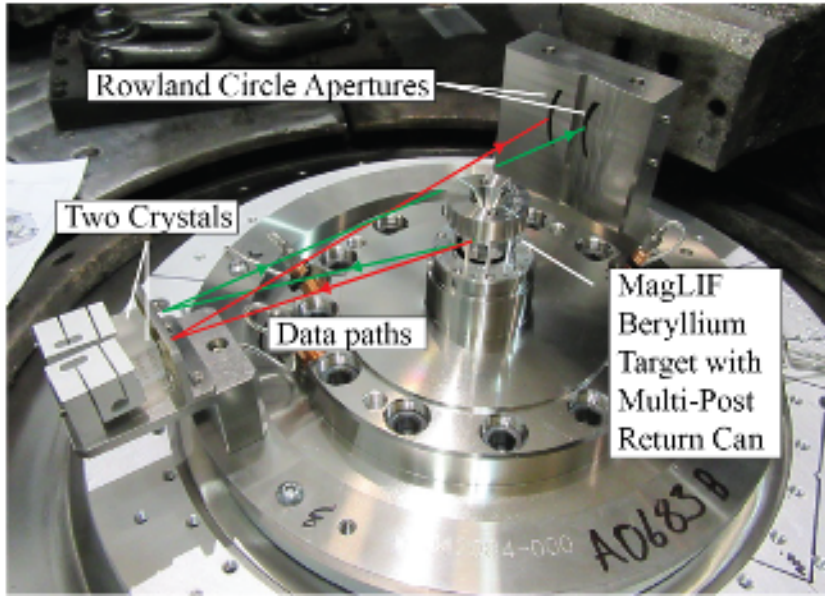

MagLIF "Laser-only" Target

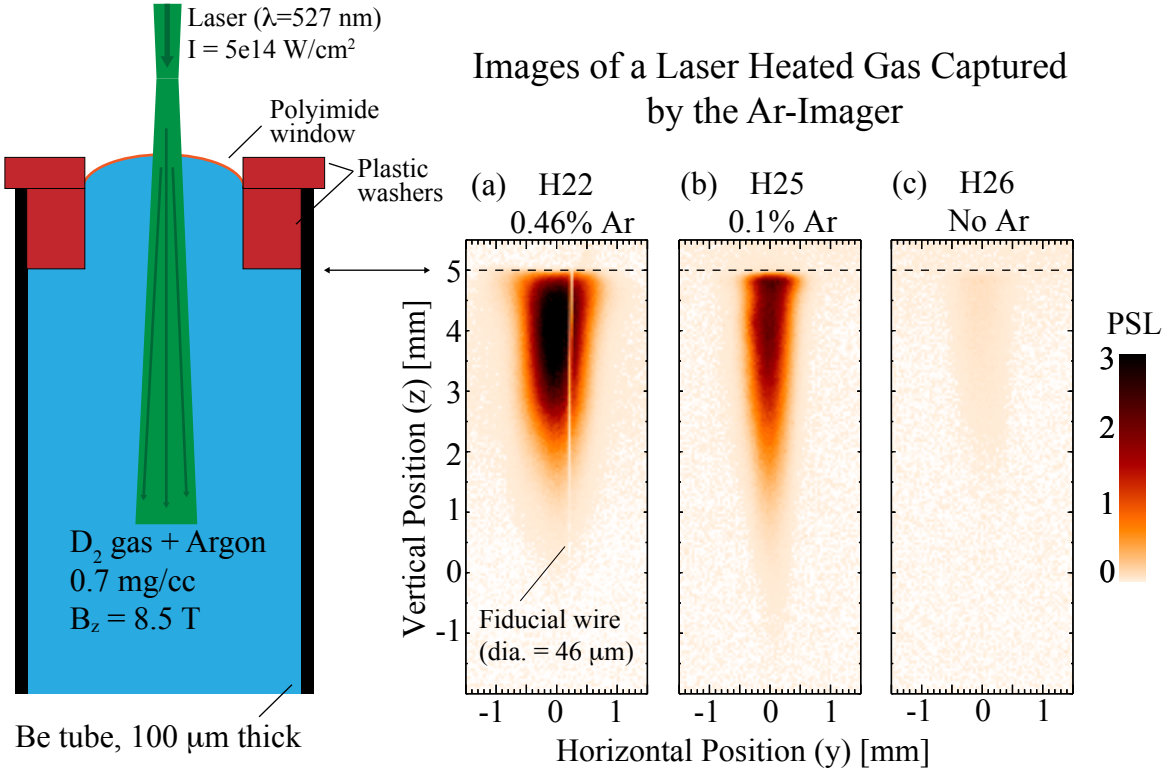

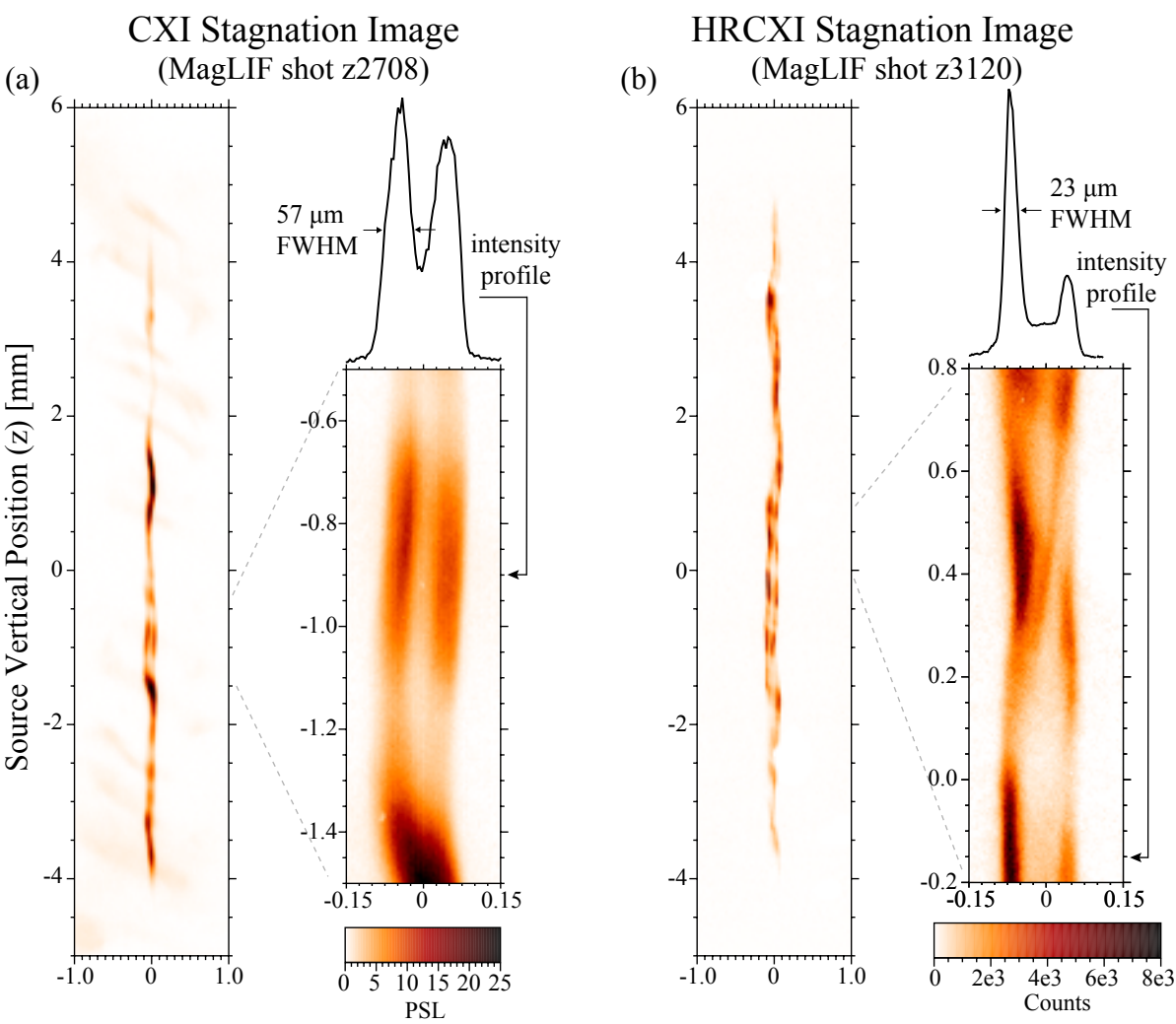
CXI Stagnation Image
(MagLIF shot z2708)
(a)
57 μm
FWHM
intensity
profile
HRCXI Stagnation Image
(MagLIF shot z3120)
(b)
23 μm
FWHM
intensity
profile
Source Vertical Position (z) [mm]
Source Horizontal Position (y) [mm]
PSL
Counts

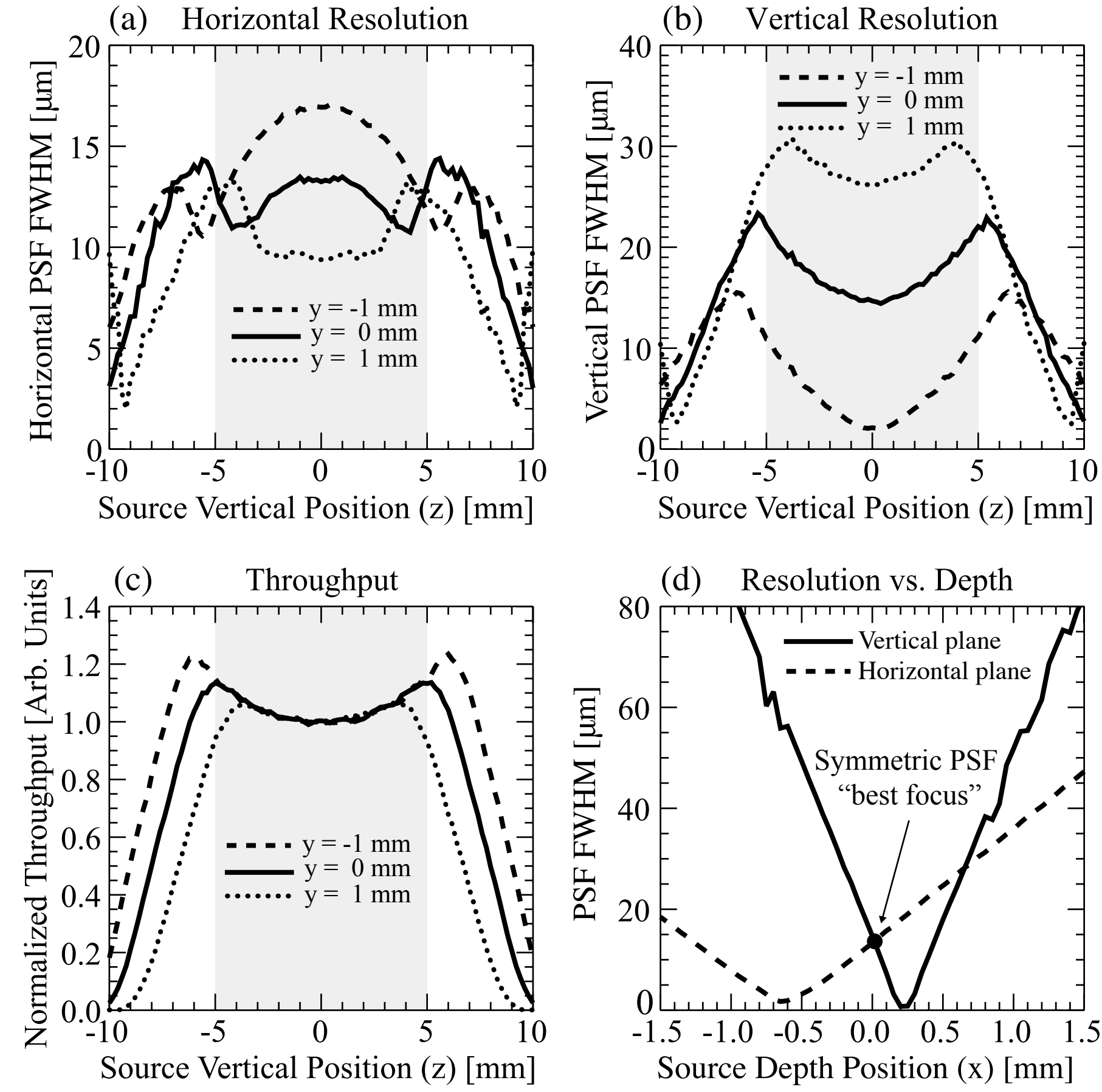
(a) Horizontal Resolution
Horizontal PSF FWHM [μm]
Source Vertical Position (z) [mm]
y = -1 mm
y = 0 mm
y = 1 mm
(b) Vertical Resolution
Vertical PSF FWHM [μm]
Source Vertical Position (z) [mm]
y = -1 mm
y = 0 mm
y = 1 mm
(c) Throughput
Normalized Throughput [Arb. Units]
Source Vertical Position (z) [mm]
y = -1 mm
y = 0 mm
y = 1 mm
(d) Resolution vs. Depth
PSF FWHM [μm]
Source Depth Position (x) [mm]
Vertical plane
Horizontal plane
Symmetric PSF
"best focus"

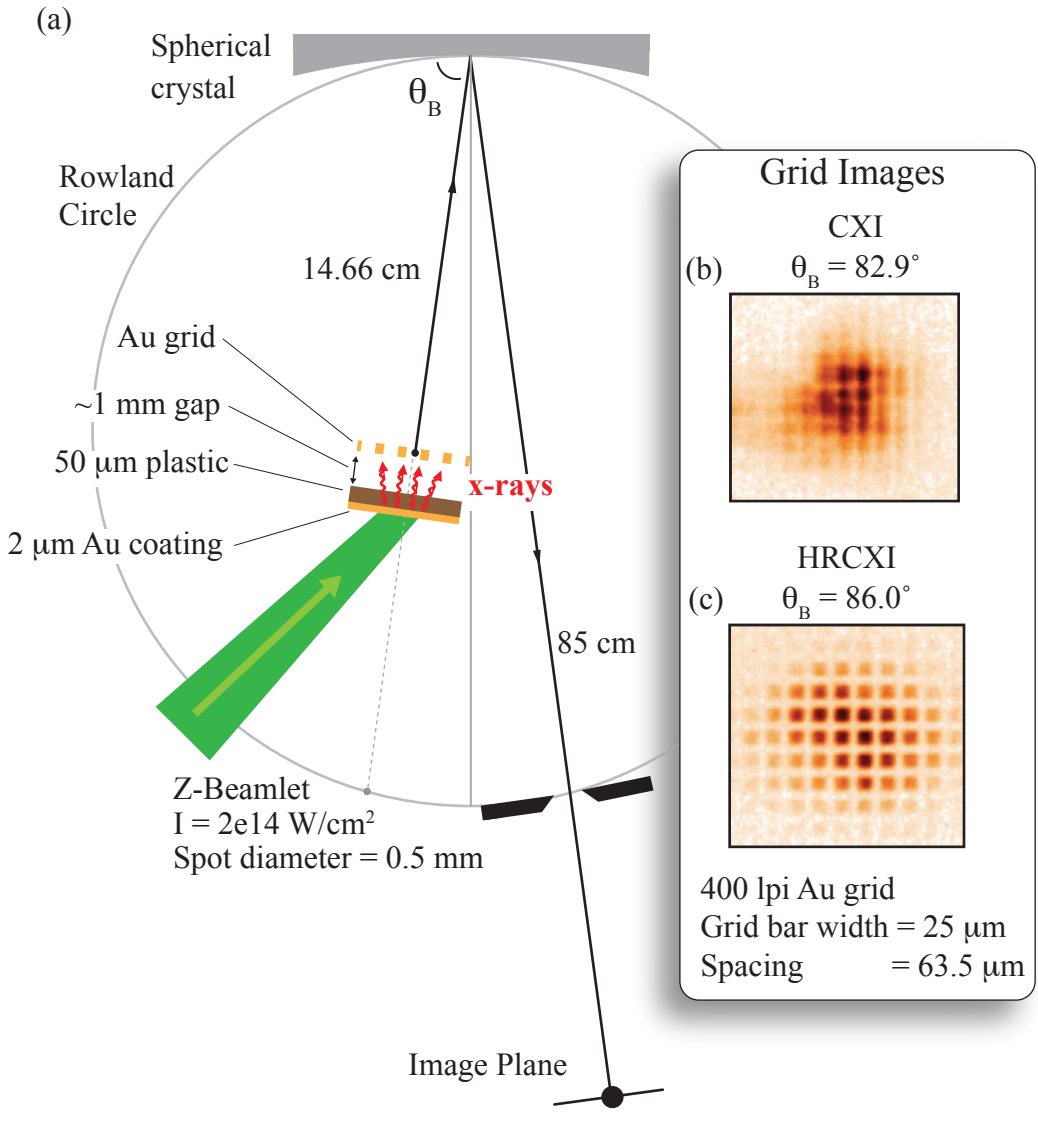
(a)
Spherical crystal
θ_B
Rowland Circle
14.66 cm
Au grid
~1 mm gap
50 μm plastic
2 μm Au coating
x-rays
85 cm
Z-Beamlet
I = 2e14 W/cm^2
Spot diameter = 0.5 mm
Image Plane
Grid Images
CXI
(b) θ_B = 82.9°
HRCXI
(c) θ_B = 86.0°
400 lpi Au grid
Grid bar width = 25 μm
Spacing = 63.5 μm

(a) Front View of Grid

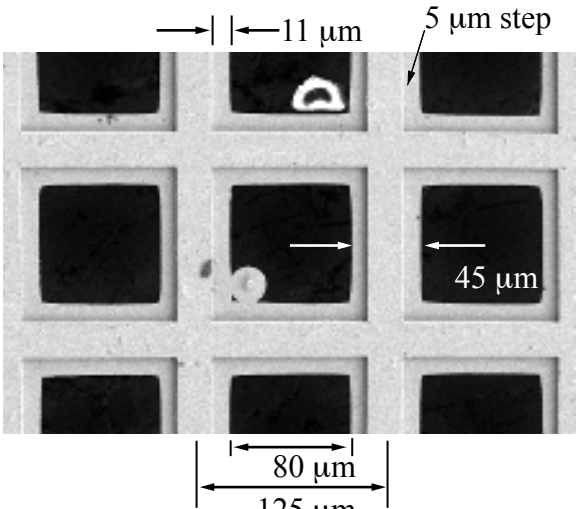

(b) Rear View of Grid

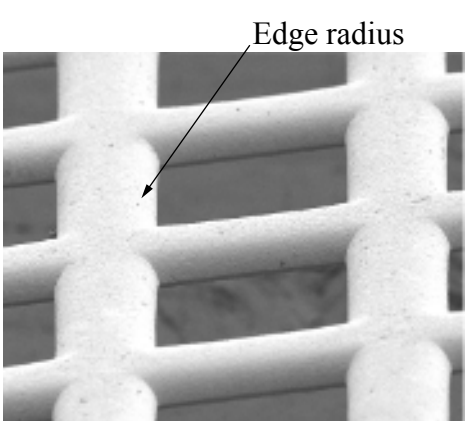

(c) Estimated Cross-Section of a Single Grid Bar

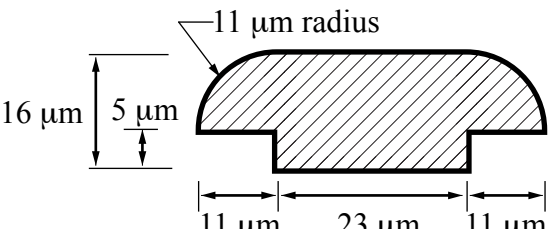

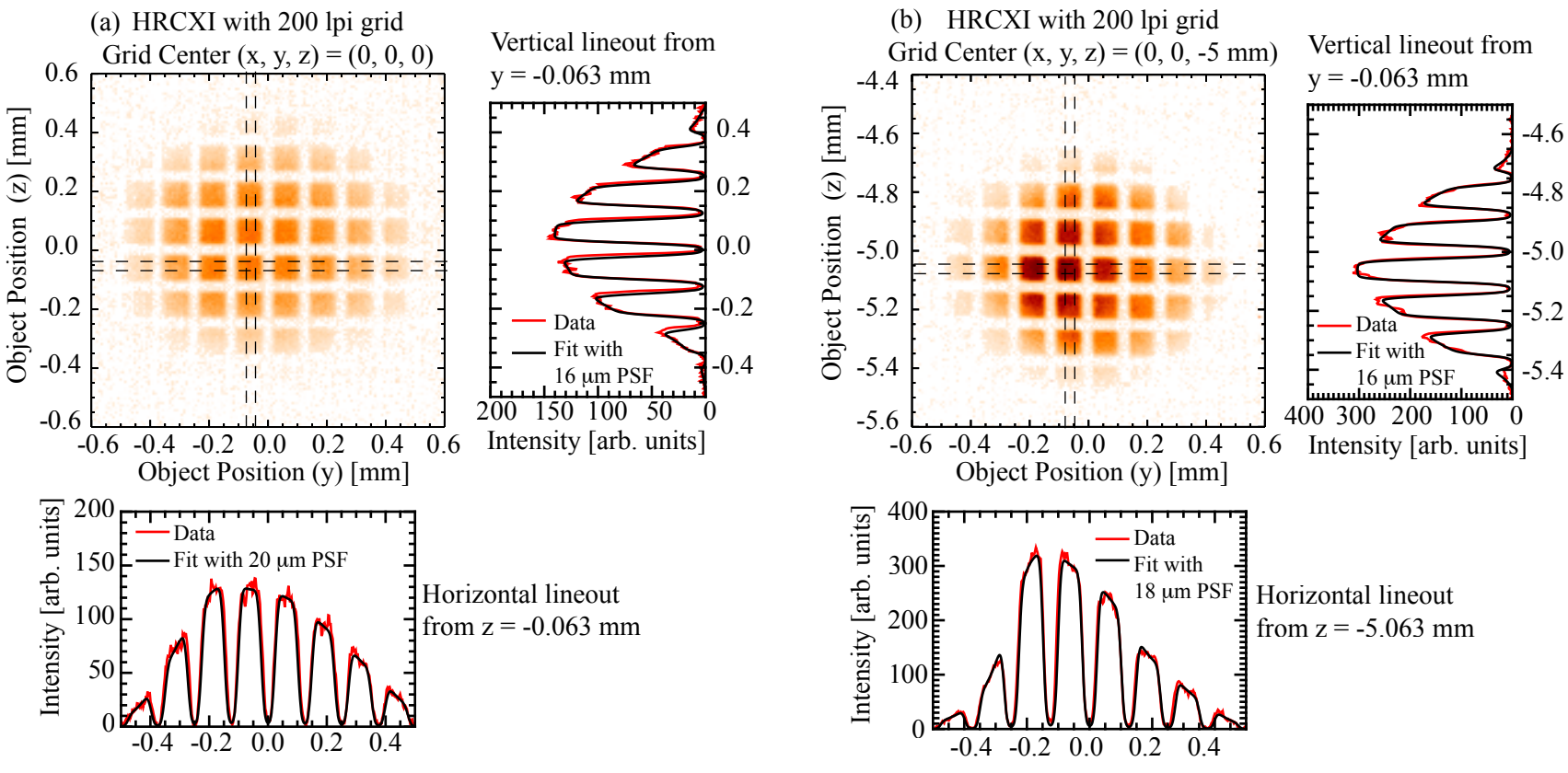
(a) HRCXI with 200 lpi grid
Grid Center (x, y, z) = (0, 0, 0)
Object Position (z) [mm]
Object Position (y) [mm]
Vertical lineout from
y = -0.063 mm
Data
Fit with
16 μm PSF
Intensity [arb. units]
Data
Fit with 20 μm PSF
Intensity [arb. units]
Horizontal lineout
from z = -0.063 mm
(b) HRCXI with 200 lpi grid
Grid Center (x, y, z) = (0, 0, -5 mm)
Object Position (z) [mm]
Object Position (y) [mm]
Vertical lineout from
y = -0.063 mm
Data
Fit with
16 μm PSF
Intensity [arb. units]
Data
Fit with
18 μm PSF
Intensity [arb. units]
Horizontal lineout
from z = -5.063 mm

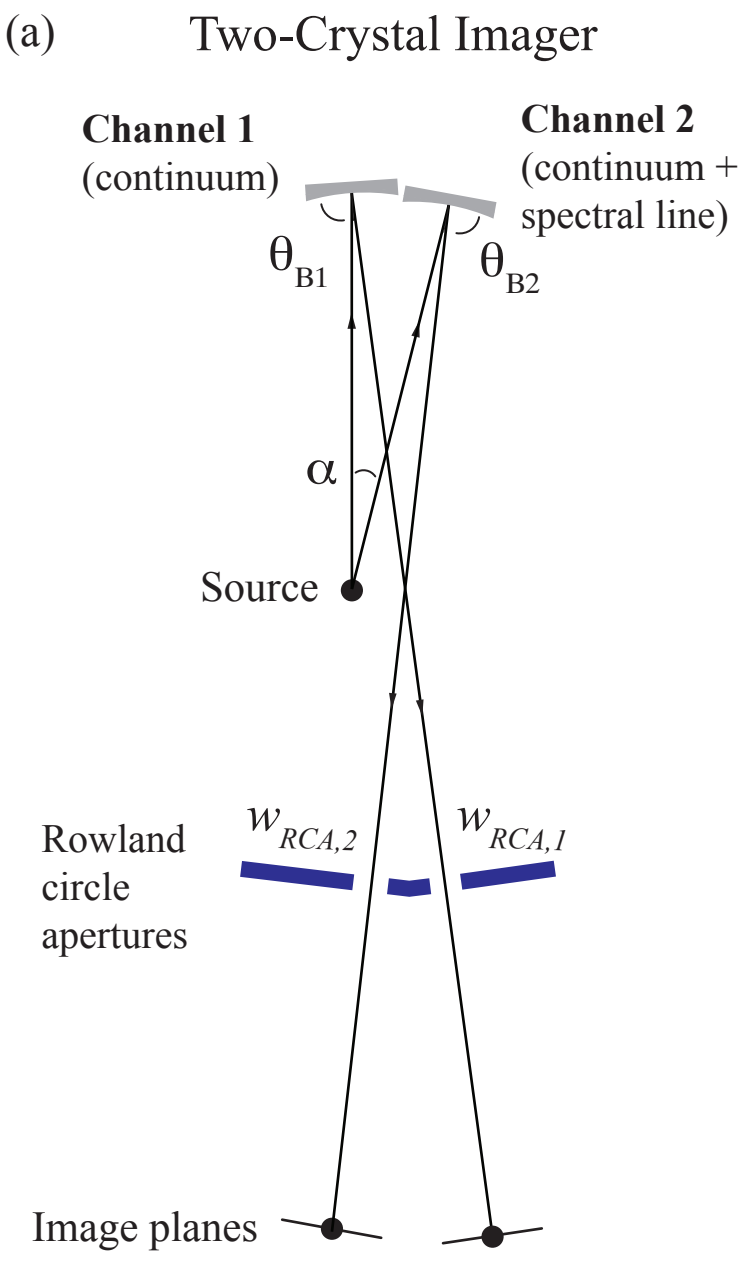
(a)
Two-Crystal Imager
Channel 1
(continuum)
Channel 2
(continuum +
spectral line)
θB1
θB2
α
Source
Rowland
circle
apertures
wRCA,2
wRCA,1
Image planes

(b) X-ray Spectrum Observed by the CHEWI Two-Crystal Imager

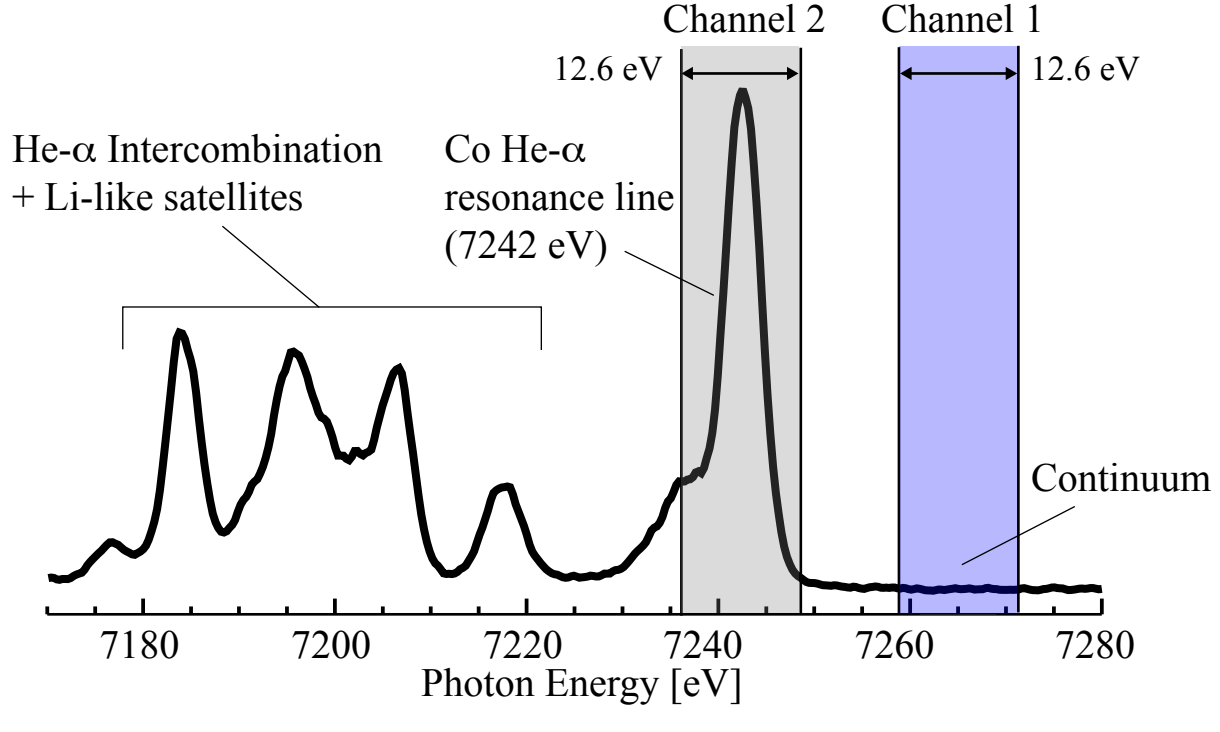

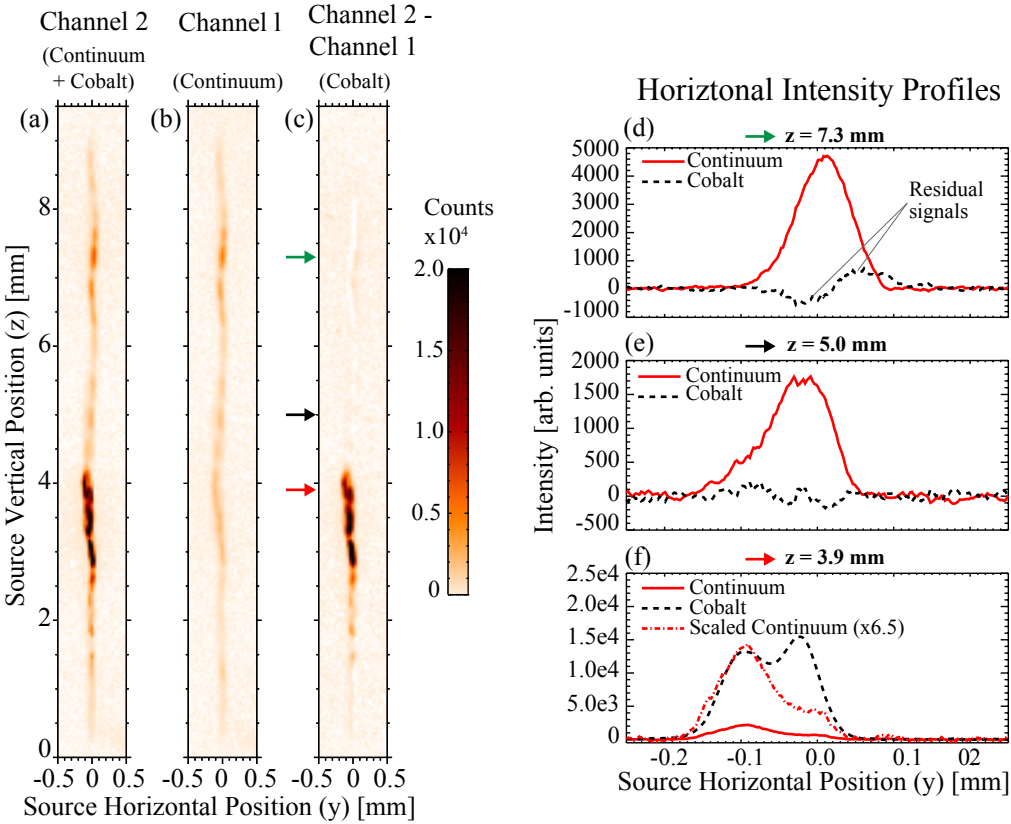
Channel 2
(Continuum
+ Cobalt)
Channel 1
(Continuum)
Channel 2 -
Channel 1
(Cobalt)
(a)
(b)
(c)
Counts
x10^4
2.0
1.5
1.0
0.5
0
Source Vertical Position (z) [mm]
Source Horizontal Position (y) [mm]
Horiztonal Intensity Profiles
(d)
z = 7.3 mm
Continuum
Cobalt
Residual
signals
(e)
z = 5.0 mm
Continuum
Cobalt
(f)
z = 3.9 mm
Continuum
Cobalt
Scaled Continuum (x6.5)
Intensity [arb. units]
Source Horizontal Position (y) [mm]

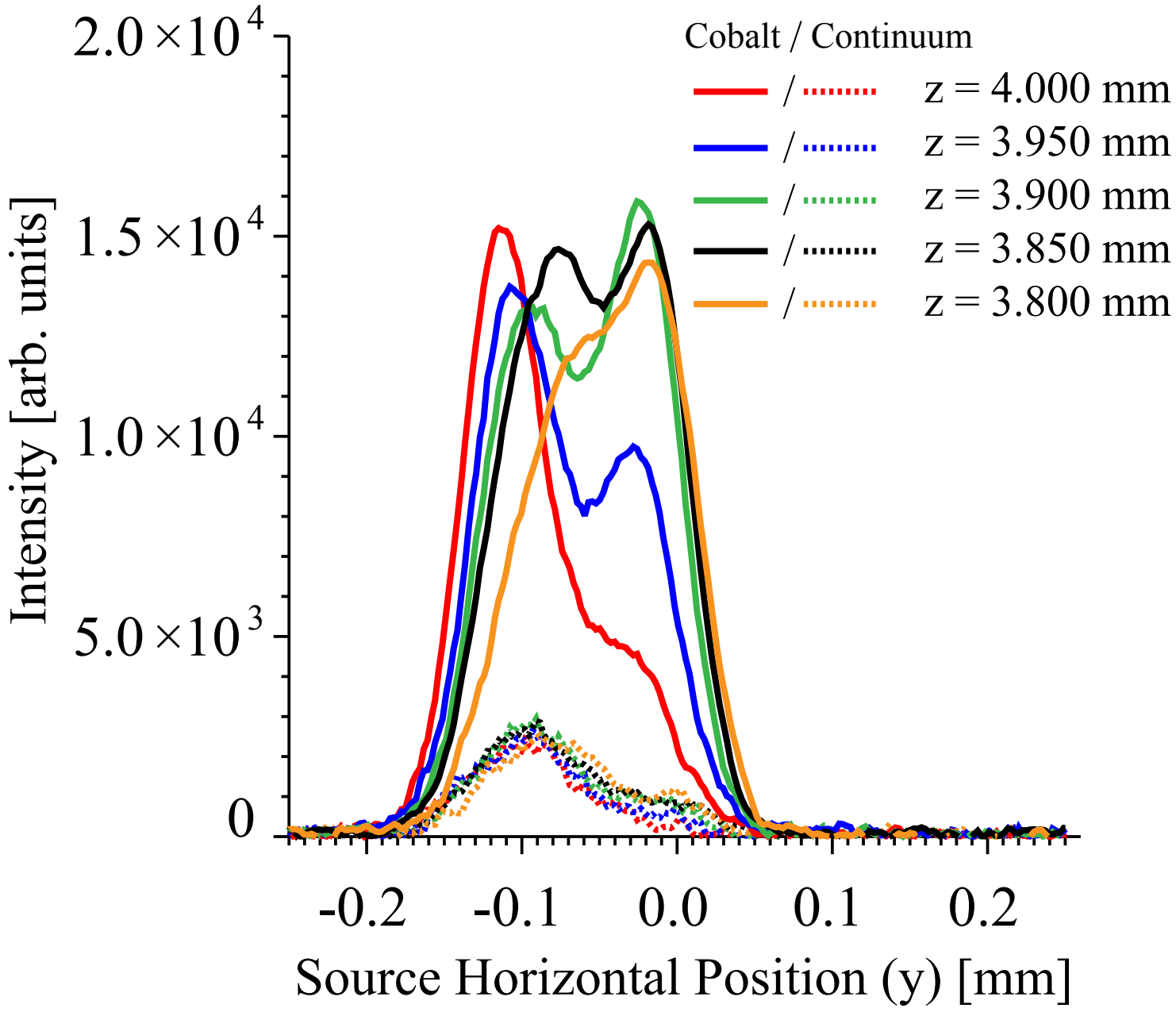
Cobalt / Continuum
z = 4.000 mm
z = 3.950 mm
z = 3.900 mm
z = 3.850 mm
z = 3.800 mm
Intensity [arb. units]
2.0×10^4
1.5×10^4
1.0×10^4
5.0×10^3
0
-0.2
-0.1
0.0
0.1
0.2
Source Horizontal Position (y) [mm]